Computer Physics Communications 185 (2014) 2412–2426

Contents lists available at ScienceDirect

Computer Physics Communications

journal homepage: www.elsevier.com/locate/cpc

On the accuracy assessment of Laplacian models in MPS

K.C. Ng [a,1], Y.H. Hwang [b], T.W.H. Sheu [c,*]

[a] Center of Advanced Computational Engineering (CACE), Department of Mechanical Engineering, Universiti Tenaga Nasional, Jalan IKRAM-UNITEN, 43000 Kajang, Selangor, Malaysia

[b] Department of Marine Engineering, National Kaohsiung Marine University, Kaohsiung 805, Taiwan

[c] Center for Advanced Studies in Theoretical Sciences (CASTS), National Taiwan University, Taipei, Taiwan

ARTICLE INFO

Article history:
Received 22 November 2013
Received in revised form
11 April 2014
Accepted 9 May 2014
Available online 27 May 2014

Keywords:
MPS
Laplacian model
Particle method
Poisson equation
Consistency
CFD

ABSTRACT

From the basis of the Gauss divergence theorem applied on a circular control volume that was put forward by Isshiki (2011) in deriving the MPS-based differential operators, a more general Laplacian model is further deduced from the current work which involves the proposal of an altered kernel function. The Laplacians of several functions are evaluated and the accuracies of various MPS Laplacian models in solving the Poisson equation that is subjected to both Dirichlet and Neumann boundary conditions are assessed. For regular grids, the Laplacian model with smaller N is generally more accurate, owing to the reduction of leading errors due to those higher-order derivatives appearing in the modified equation. For irregular grids, an optimal N value does exist in ensuring better global accuracy, in which this optimal value of N will increase when cases employing highly irregular grids are computed. Finally, the accuracies of these MPS Laplacian models are assessed in an incompressible flow problem.

1. Introduction

In the numerical framework of the Moving Particle Semi-implicit (MPS) method, the differential terms appearing in the Navier–Stokes equation are represented by particle interaction models, i.e. gradient and Laplacian models. The gradient model is mainly used to discretize the pressure gradient term appeared in the momentum equations. In order to alleviate the issue due to the overestimation of inter-particle attractive forces associated with the particle method, numerous efforts have been paid to develop a stable and accurate gradient operator: the Minimum pressure model [1], the CMPS model [2], the Corrective Matrix model [3] and the most recent Dynamic Stabilization model [4]. On the other hand, the Laplacian model is mainly employed to evaluate the viscous stresses (from the explicit computation of Laplacian of an existing velocity field) as well as to discretize the Poisson equation of pressure, whereby the pressure field is primarily driven by the density imbalance (appeared as the source term) and the prescribed boundary conditions, which is more commonly known as the Boundary Value Problem (BVP). The associated open literatures detailing on the refinement of the original MPS Laplacian operator, however, are rather limited. From the authors' point of view, in order to enhance the overall robustness of a MPS scheme, the development of a more reliable Laplacian operator must not be overlooked.

The original Laplacian model was proposed by Koshizuka et al. [5], whereby this model is inspired from the analytical solution of the transient diffusion problem (Gaussian function). By introducing the diffusion coefficient denoted as λ, this model ensures that the increase in variance is equivalent to that of the analytical solution. Duan and Chen [6] have recently detailed on how the original Laplacian model is related to that based on the Gaussian function. On the other hand, Isshiki [7] has adopted the Gauss divergence theorem (applied to a circular control volume) and successfully reproduced the original MPS-based gradient and Laplacian models. The original Laplacian model has been successfully applied to numerous engineering applications such as breaking waves [1,8,9], complex thermal-hydraulic flow [10], steel-making process [11], fluid–structure interaction [12–14], mixing problem [15,16] and many others. Besides that, the modeling of anisotropic diffusion (multiple fluid viscosity) within the framework of the original Laplacian model has been considered as well for multiphase flow simulation [17–20]. Very recently, Souto-Iglesias et al. [21] have addressed on the inconsistency issue of the

* Corresponding author. Tel.: +886 2 33665746; fax: +886 2 23929885.
E-mail addresses: ngkhaiching2000@yahoo.com (K.C. Ng), yhhwang@webmail.nkmu.edu.tw (Y.H. Hwang), twhsheu@ntu.edu.tw (T.W.H. Sheu).
[1] Tel.: +60 389212020x6478.

http://dx.doi.org/10.1016/j.cpc.2014.05.012
0010-4655/

original Laplacian model near the boundary and they have circumvented this problem by using a boundary correction scheme.

Although the original Laplacian model has enjoyed reasonable success in MPS computation, Zhang et al. [22,23] have argued on the mathematical inconsistency of the diffusion coefficient λ appearing in the original Laplacian model. They have reported that numerical difficulties will arise when the Poisson equation is solved. By dropping the diffusion coefficient term, a new Laplacian model (denoted as Zhang's model in this paper) has been derived by them and it has been successfully applied to a transient heat conduction problem. As reported by Zhang et al. [23], the accuracy of their new Laplacian model is indeed better as compared to that of the original one. Although its popularity is not comparable to that of the original Laplacian model, this model has been widely adopted as well in some engineering applications such as convective heat transfer problem [24], turbomachinery [25], pressure wave transmission [26], MHD problems [27,28] and solid mechanics [29,30]. Recently, Sheu et al. [31] and Huang and Sheu [32,33] have applied their newly developed kernel function in the Zhang's model and they have successfully computed a wide range of incompressible flow problems.

Inspired by the idea from Smoothed Particle Hydrodynamics (SPH) whereby the gradient is expressed as a function of the first derivative of a kernel function, Khayyer and Gotoh [34] have formulated a new Laplacian model (the so-called Higher-order Laplacian (HL) model) based on the divergence of the SPH gradient operator. Although this model is not widely employed within the MPS community due to the fact that it is relatively new as compared to the other Laplacian models, Khayyer and Gotoh [34] have demonstrated that the HL model can produce a smoother pressure field. Recently, Khayyer and Gotoh [35] have extended their HL model to 3D environment.

In spite of the fact that these Laplacian models have received distinct degrees of acceptance within the MPS community, the underlying reason leading to an inclination of a research group to implement a specific Laplacian model in their MPS solver has not been fully understood. Particularly, the detailed study addressing on the accuracies of various Laplacian models in evaluating the Laplacian term as well as solving the Poisson equation is rather limited. Besides that, the accuracies of the Laplacian models in both the regular and irregular grid structures have not been carefully assessed as well in the open literature. In this paper, we attempt to assess the accuracies of these MPS-based Laplacian models (derivative of the kernel function is not required) on both the regular and irregular grid structures. During the course of the current work, a more general Laplacian model is derived, whereby the original Laplacian model and the Zhang's model can indeed be deduced from this general MPS-based Laplacian model. Also, by performing the modified equation analysis on this general Laplacian model, a more accurate Laplacian model particularly in the context of regular grid structure can indeed be recovered.

2. Derivation of the general MPS Laplacian model

In this Section, the mathematical background of a MPS Laplacian model is presented. Inspired by the recent work by Isshiki [7], the Gauss divergence theorem is applied on a circular control volume (say 2D for the discussion purpose) illustrated in Fig. 1:

$$\int \nabla^2\varphi dV = \int \varphi_x dA_x + \int \varphi_y dA_y. \tag{1}$$

For a circular control volume, the differential area vector originated from the boundary is:

$$\langle dA_x, dA_y\rangle = dl\left\langle \frac{x_{ik}}{r_{ik}}, \frac{y_{ik}}{r_{ik}}\right\rangle. \tag{2}$$

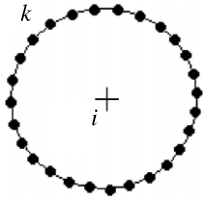

Fig. 1. Schematic of a circular control volume with radius r_{ik}.

Here, x_{ik} is $x_k - x_i$ and y_{ik} is $y_k - y_i$. r_{ik} denotes the distance between particles i and k. dl is the segmental arc length of the circular boundary:

$$dl = \frac{P_{ik}}{N_{ik}}, \tag{3}$$

where P_{ik} and N_{ik} are the perimeter and number of particles residing at a circular boundary with radius r_{ik}, respectively. Substituting Eq. (2) into Eq. (1) gives

$$\begin{aligned}\int \nabla^2\varphi dV &= \int \left(\varphi_x \frac{x_{ik}}{r_{ik}} + \varphi_y \frac{y_{ik}}{r_{ik}}\right) dl \\ &= \int \left(\frac{\partial\varphi}{\partial r}\frac{\partial r}{\partial x}\frac{x_{ik}}{r_{ik}} + \frac{\partial\varphi}{\partial r}\frac{\partial r}{\partial y}\frac{y_{ik}}{r_{ik}}\right) dl \\ &= \int \left(\frac{\partial\varphi}{\partial r}\frac{x_{ik}^2}{r_{ik}^2} + \frac{\partial\varphi}{\partial r}\frac{y_{ik}^2}{r_{ik}^2}\right) dl \\ &= \int \frac{\partial\varphi}{\partial r} dl.\end{aligned} \tag{4}$$

Now, Eq. (4) can be discretized as:

$$V_{ik}\langle\nabla^2\varphi_i\rangle = \beta \sum_k \frac{\varphi_k - \varphi_i}{r_{ik}}\frac{P_{ik}}{N_{ik}}. \tag{5}$$

Here, V_{ik} is the volume of the circular control volume with radius r_{ik}. β is the correction factor (=2.0) to compensate for the error generated due to the one-sided differencing scheme applied for the approximation of radial derivative at the boundary. By rearranging Eq. (5), the following is obtained:

$$N_{ik}\langle\nabla^2\varphi_i\rangle = \beta\frac{P_{ik}}{V_{ik}}\sum_k \frac{\varphi_k - \varphi_i}{r_{ik}} = \beta\frac{d}{r_{ik}}\sum_k \frac{\varphi_k - \varphi_i}{r_{ik}}. \tag{6}$$

It can be easily shown that P/V is d/r where d is the number of dimensions. In the current work, both the parameter r_{ik}^N and weight w_{ik} are introduced on both sides of Eq. (6), thereby leading to:

$$N_{ik}w_{ik}r_{ik}^N\langle\nabla^2\varphi_i\rangle = \sum_k w_{ik}r_{ik}^N\langle\nabla^2\varphi_i\rangle = 2d\sum_k(\varphi_k - \varphi_i)r_{ik}^{N-2}w_{ik}. \tag{7}$$

Henceforth, Eq. (7) is applied for different radius ranging from $r_{ik} = 0$ to $r_{ik} = R$. Here, R is termed the radius of influence in MPS. Upon summation of Eq. (7) at different radii, a general Laplacian operator can be recovered:

$$\langle\nabla^2\varphi_i\rangle = \frac{2d}{\sum_{i\neq j} w^*(|\vec{r}_j - \vec{r}_i|)}\sum_{i\neq j}\frac{(\varphi_j - \varphi_i)}{|\vec{r}_j - \vec{r}_i|^2}w^*(|\vec{r}_j - \vec{r}_i|), \tag{8}$$

where $w^*(|\vec{r}_j - \vec{r}_i|) = |\vec{r}_j - \vec{r}_i|^N w(|\vec{r}_j - \vec{r}_i|)$ can be interpreted as a modified kernel function in the general Laplacian model. It is important to note from Eq. (8) that the original Laplacian model [5] and the Zhang's model [23] can be recovered by assigning the values of $N = 2$ and $N = 0$, respectively. The kernel function $w(|\vec{r}_j - \vec{r}_i|)$ reported by Koshizuka et al. [1] is employed in the current work.

3. Modified equation analysis

In the regular grid environment, the Laplacian operator $\langle\nabla^2\varphi\rangle$ can be discretized by using Eq. (8). Following this, the 2D Laplacian at lattice point (i, j) can be expressed as:

$$\begin{aligned}\langle\nabla^2\varphi\rangle = &\frac{4}{4w(s)s^N + 4w(\sqrt{2}s)(\sqrt{2}s)^N}\\ &\times\left[w(s)s^{N-2}\left(\varphi_{i,j+1}+\varphi_{i,j-1}+\varphi_{i-1,j}+\varphi_{i+1,j}-4\varphi_{i,j}\right)\right.\\ &+w(\sqrt{2}s)(\sqrt{2}s)^{N-2}\left(\varphi_{i-1,j+1}+\varphi_{i+1,j-1}+\varphi_{i-1,j-1}\right.\\ &\left.\left.+\varphi_{i+1,j+1}-4\varphi_{i,j}\right)\right].\end{aligned} \tag{9}$$

Here, s is the grid spacing and $R = 2s$. By approximating the neighboring terms (e.g. $\varphi_{i+1,j}$, $\varphi_{i+1,j+1}$ etc.) in Eq. (9) relative to the local term $\varphi_{i,j}$ with Taylor series, the following equation can be obtained:

$$\begin{aligned}&\langle\nabla^2\varphi\rangle\\ &=\frac{1}{\left(w(s)+w(\sqrt{2}s)(\sqrt{2})^N\right)s^2}\left[\left(w(s)+w(\sqrt{2}s)(\sqrt{2})^N\right)\right.\\ &\times\left[\frac{\partial^2\varphi}{\partial x^2}s^2+\frac{\partial^2\varphi}{\partial y^2}s^2\right]+\left(w(s)+w(\sqrt{2}s)(\sqrt{2})^N\right)\\ &\times\left(\frac{1}{12}\frac{\partial^4\varphi}{\partial x^4}s^4+\frac{1}{12}\frac{\partial^4\varphi}{\partial y^4}s^4\right)+w(\sqrt{2}s)(\sqrt{2})^{N-2}\frac{\partial^4\varphi}{\partial x^2\partial y^2}s^4\\ &+\left(w(s)+w(\sqrt{2}s)(\sqrt{2})^N\right)\left(\frac{1}{360}\frac{\partial^6\varphi}{\partial x^6}s^6+\frac{1}{360}\frac{\partial^6\varphi}{\partial y^6}s^6\right)\\ &\left.+w(\sqrt{2}s)(\sqrt{2})^{N-2}\left(\frac{1}{12}\frac{\partial^6\varphi}{\partial x^4\partial y^2}s^6+\frac{1}{12}\frac{\partial^6\varphi}{\partial x^2\partial y^4}s^6\right)+\cdots\right].\end{aligned} \tag{10}$$

The above modified equation (or equivalent PDE) can be rearranged as

$$\begin{aligned}\langle\nabla^2\varphi\rangle = &\frac{\partial^2\varphi}{\partial x^2}+\frac{\partial^2\varphi}{\partial y^2}\\ &+\left(\frac{1}{12}\frac{\partial^4\varphi}{\partial x^4}+\frac{1}{12}\frac{\partial^4\varphi}{\partial y^4}+\frac{\partial^4\varphi}{\partial x^2\partial y^2}\underbrace{\left\{\frac{w(\sqrt{2}s)(\sqrt{2})^{N-2}}{w(s)+w(\sqrt{2}s)(\sqrt{2})^N}\right\}}_{A}\right)s^2\\ &+\left(\frac{1}{360}\frac{\partial^6\varphi}{\partial x^6}+\frac{1}{360}\frac{\partial^6\varphi}{\partial y^6}+\frac{1}{12}\left[\frac{\partial^6\varphi}{\partial x^2\partial y^4}+\frac{\partial^6\varphi}{\partial x^4\partial y^2}\right]\right.\\ &\left.\times\underbrace{\left\{\frac{w(\sqrt{2}s)(\sqrt{2})^{N-2}}{w(s)+w(\sqrt{2}s)(\sqrt{2})^N}\right\}}_{A}\right)s^4+\cdots.\end{aligned} \tag{11}$$

It can be observed from Eq. (11) that the following limits hold true upon applying the l'hopital's rule:

$$\lim_{N\to-\infty}A=\lim_{N\to-\infty}\frac{w(\sqrt{2}s)(\sqrt{2})^{N-2}}{w(s)+w(\sqrt{2}s)(\sqrt{2})^N}=0, \tag{12}$$

$$\lim_{N\to\infty}A=\lim_{N\to\infty}\frac{w(\sqrt{2}s)(\sqrt{2})^{N-2}}{w(s)+w(\sqrt{2}s)(\sqrt{2})^N}=\frac{1}{2}. \tag{13}$$

Fig. 2 depicts graphically the variation of A with respect to N. Seemingly, as N is decreasing, the magnitude of A is diminishing and approaching the lower asymptote ($A = 0$). In short, the leading errors due to higher-order cross derivative terms appeared in Eq. (11) could be effectively eliminated if $N \ll 0$. For 1D problem, smaller N plays a significant role in reducing the leading errors due to higher-order derivatives. This may explain on the earlier observation reported by Zhang et al. [23], whereby they have witnessed the superior accuracy of the Zhang's model ($N = 0$) against the original Laplacian model ($N = 2$) particularly in the case of regular grid structure.

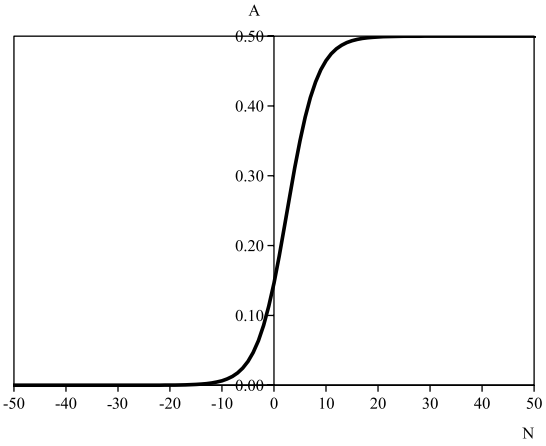

Fig. 2. The relation of A and N in the general MPS Laplacian model. $R = 2s$. Kernel function of Koshizuka et al. [1] is used.

In the context of irregular grids, it is difficult to attain the accuracy order of $O(s^k)$, where k is a positive number ($k = 2$ for regular grids shown in Eq. (11)), due to the following reason:

$$\begin{aligned}\langle\nabla^2\varphi\rangle = &\underbrace{\frac{4\Omega_2^{1,0}}{\Omega_0^{0,0}}}_{AV_x}\frac{\partial\varphi}{\partial x}+\underbrace{\frac{4\Omega_2^{0,1}}{\Omega_0^{0,0}}}_{AV_y}\frac{\partial\varphi}{\partial y}+\frac{2\Omega_2^{2,0}}{\Omega_0^{0,0}}\frac{\partial^2\varphi}{\partial x^2}\\ &+\frac{2\Omega_2^{0,2}}{\Omega_0^{0,0}}\frac{\partial^2\varphi}{\partial y^2}+\frac{4\Omega_2^{1,1}}{\Omega_0^{0,0}}\frac{\partial^2\varphi}{\partial x\partial y}+O(s),\end{aligned} \tag{14}$$

where AV_x and AV_y are termed the artificial velocities in x- and y-directions, respectively. Consistency can be ensured if $\Omega_2^{1,0} = \Omega_2^{0,1} = \Omega_2^{1,1} = 0$ and $\Omega_2^{2,0} = \Omega_2^{0,2} = 0.5\Omega_0^{0,0}$, which is satisfied in the case of regular grid (square or close-packed lattice). In the current work, only the square lattice is considered (for 2D) when the case of regular grid is reported in the current work. The artificial velocities may become non-zero when irregular grid is employed, thereby leading to the accuracy order of $O(s^{-1})$. This implies that the numerical accuracy of MPS Laplacian operator cannot be further improved by refining the particle spacing s, as will be observed later in the current work. Here, $\Omega_m^{p,q}$ is the geometric operator, defined as:

$$\Omega_m^{p,q}=\sum_{i\neq j}\frac{(x_j-x_i)^p(y_j-y_i)^q w^*\left(\left|r_j-r_i\right|\right)}{\left|r_j-r_i\right|^m}. \tag{15}$$

4. Result and discussion

In this Section, the particle interaction model expressed in Eq. (8) will be used to evaluate the Laplacian of a given function as well as discretize the Poisson equation subjected to different boundary conditions. The accuracies of various Laplacian models deduced from this general model (Eq. (8)) are accessed. Finally, the accuracies of various Laplacian models in simulating an incompressible flow problem are reported.

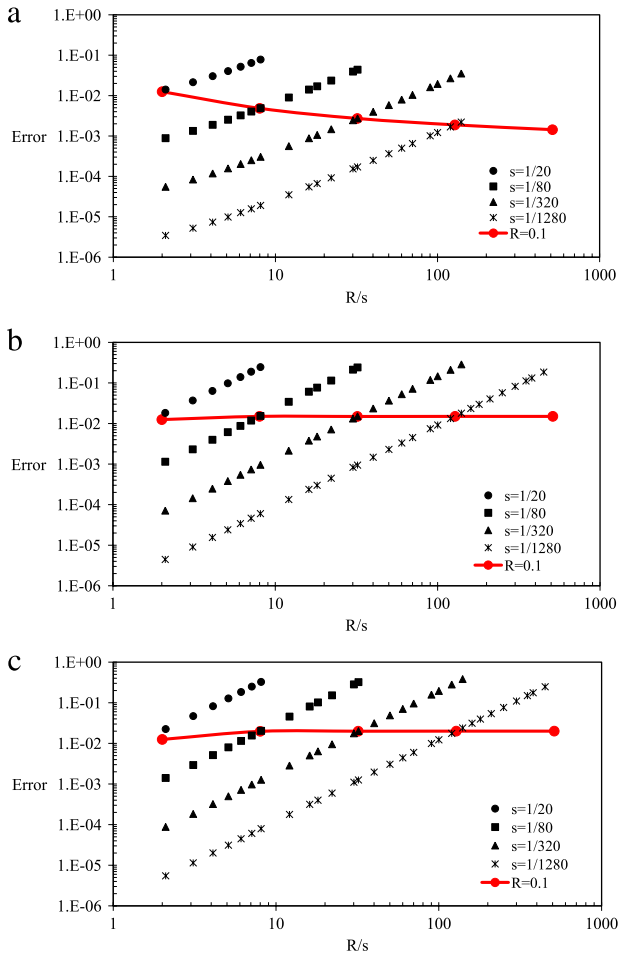

Fig. 3. Plot of errors with respect to R/s by using (a) $N = 0$, (b) $N = 2$ and (c) $N = 3$ models on the L1 problem. Regular grid with different particle spacings s is used.

4.1. Laplacian evaluation

4.1.1. Regular grid

In this Section, the Laplacian of several functions are explicitly evaluated by the proposed general MPS Laplacian model. Let us consider a non-linear field (denoted as the L1 problem): $G(x) = x^5$ for $x \in [0, 1]$. Here, the boundary effects are negated, whereby the Laplacian (G_{xx}) is evaluated only at the interior particles (total number is N_{int}), i.e. $x \in [R, 1 - R]$. The averaged error is computed as: $\sum_{int} \left|G_{xx,comp} - G_{xx,abs}\right| / N_{int}$, where $G_{xx,comp}$ and $G_{xx,abs}$ are the computed and the absolute Laplacian values, respectively.

Fig. 3 shows the errors generated from various Laplacian models at different regular grid spacing (s). By adopting a fixed R/s (or a fixed number of neighbor within R), the numerical model employing a smaller grid spacing yields a more accurate solution (consistency is ensured). However, in a particular regular grid system with spacing s, the error level is increasing if the number of neighbor within R increases (increasing R/s). It is worth to mention here that Souto-Iglesias et al. [21] have fixed the value of R while keeping $s \to 0$ in order to test the consistency of the original Laplacian model. Here, R is prescribed as 0.1, and the corresponding errors are overlaid (as red dots) in Fig. 3. As seen, the error level is almost constant as $s \to 0$ for $N = 2$ (original Laplacian model) and $N = 3$ models, while the error level of Zhang's model ($N = 0$) is decaying as the grid is refined.

Fig. 4 compares the accuracies of various Laplacian models for $N \in [-10, 50]$ employing grid spacing $s = 1/320$. As expected, the

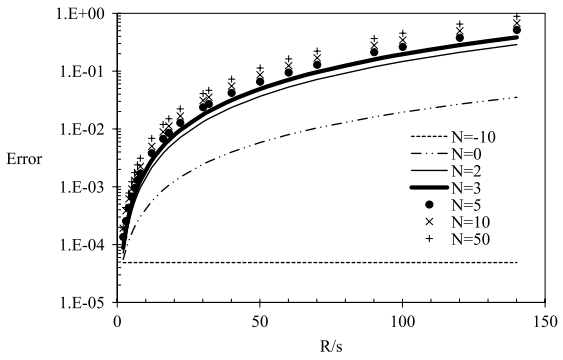

Fig. 4. Plot of errors with respect to R/s by using various Laplacian models on the L1 problem. Regular grid with $s = 1/320$ is used.

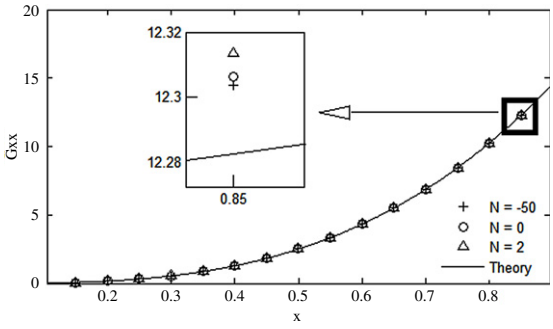

Fig. 5. Predicted Laplacian for the L1 problem on a regular grid with $s = 1/20$. $R/s = 2.1$.

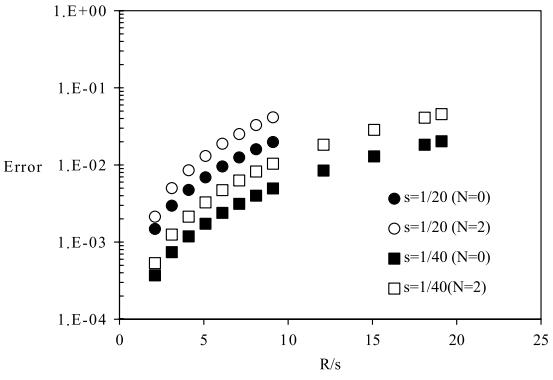

Fig. 6. Plot of errors with respect to R/s on L2 problem for $N = 0$ and $N = 2$ models. Regular grid with different particle spacings s is used.

errors are increasing with respect to the number of neighbors (R/s). On the other hand, it is interesting to note that the error is reduced as the Laplacian models with smaller N are used regardless of the chosen R/s. As shown in Fig. 5, model of $N = -50$ shows a closer agreement with the theoretical solution, followed by the Zhang's model ($N = 0$) and the original Laplacian model ($N = 2$). The improvement in accuracy of the conventional Laplacian models when $N < 0$, albeit it is marginal at small R/s (result of $R/s = 2.1$ is shown in Fig. 5), can be further augmented if a larger R is used as reported in Fig. 4.

Next, the Laplacian of a 2D function (L2 problem): $G(x, y) = (x + 1)^2(y + 1)^2$ for $x \in [-0.5, 0.5]$; $y \in [-0.5, 0.5]$ is evaluated at point (0,0), where the theoretical solution is 4.0. The results obtained from the Zhang's model and the original Laplacian model are plotted in Fig. 6. Similar to that observed in the 1D problem, for a fixed grid spacing s, the error is increasing with respect to the number of neighbors (R/s). And, the accuracy of the original

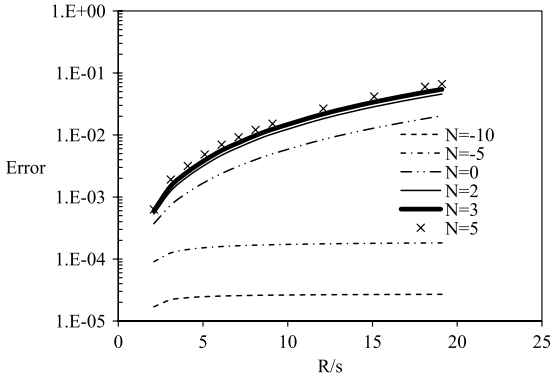

Fig. 7. Variation of errors with respect to R/s by using various Laplacian models on L2 problem. Regular grid with $s = 1/40$ is used.

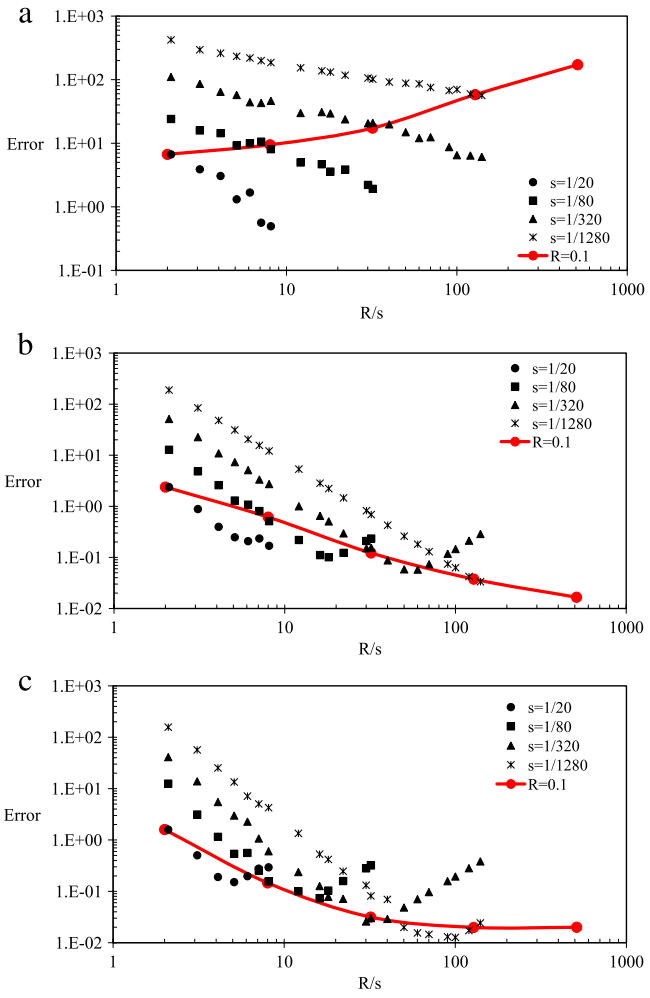

Fig. 8. Plot of errors with respect to R/s by using (a) $N = 0$, (b) $N = 2$ and (c) $N = 3$ models on the L1 problem. Irregular grid with % of randomness =10% is used.

Laplacian model is somehow inferior as compared to that of the Zhang's model. Fig. 7 shows a more comprehensive comparison of the Laplacian models; it shows a very noticeable improvement in accuracy while $N = -10$ model is employed.

4.1.2. Irregular grid

Now, the locations of the particles are slightly modified by displacing them from the original positions (regular grid position

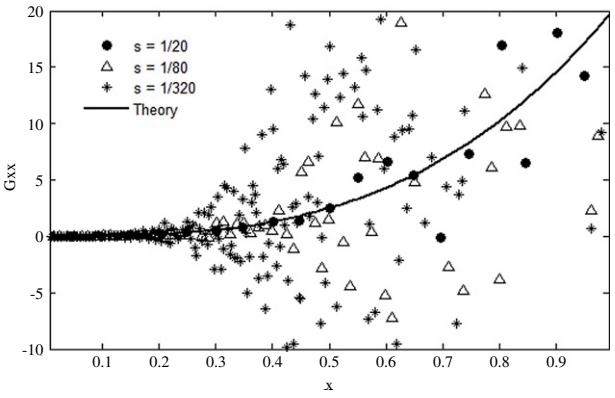

Fig. 9. Predicted Laplacian by using $N = 3$ model for the L1 problem. $R/s = 2.1$. Irregular grid with % of randomness =10% is used.

of spacing s) with a random noise of maximum amplitude equal to Ps, where P is the % of randomness. With $P = 10\%$, the L1 problem is solved again by using various Laplacian models and the results are shown in Fig. 8. Contrary to those observed on the regular grid system, for a particular grid spacing s, the averaged error (as defined in Section 4.1.1) is now constantly decreasing with respect to the number of neighbors (R/s) as deduced from the $N = 0$ model. Similarly, the averaged errors generated from the $N = 2$ and $N = 3$ models are decaying as R/s increases and experiencing a rebound (increase in error) beyond a critical R/s value. Also, it is interesting to note that the effort of reducing the grid spacing while retaining the same number of neighbor (R/s) is no longer acceptable in this case, as it shows an increase in error level at low R/s regime ($2.1 < R/s < 4.1$ is typically used in MPS) as reported in Fig. 8 (see Eq. (14) as well). Fig. 9 illustrates the augmentation in error for $N = 3$ model while refining the grid spacing in the L1 problem by retaining the parameter R/s as 2.1. As suggested in Fig. 8, if one wishes to refine the grid spacing (e.g. to capture those small scale flow structures), the radius of influence R must be correspondingly increased (more number of neighbors) in order to attain a reasonably accurate explicit calculation of the Laplacian term.

Souto-Iglesias et al. [21] have shown that the prediction of the original Laplacian model converges to the analytical solution as $s \to 0$ while keeping $R = 0.1$, even in the case of irregular grid. This phenomenon is observed as well for both the $N = 2$ and $N = 3$ models as shown in Fig. 8(b) and (c), where the error is decreasing as the grid is refined. This important property, however, is not observed in the Zhang's model ($N = 0$) as one can observe a considerably rapid increase of error level while the grid spacing is refined for a prescribed value of R. In order to illustrate this observation, the effect of grid refinement (while keeping $R = 0.1$) against the accuracy of the numerical solution is shown in Fig. 10. As seen, spurious oscillations are generated from the $N = 0$ model, while the numerical solution obtained from the original $N = 2$ model is converging to the theoretical solution as the grid spacing is refined from 1/20 to 1/320.

The numerical accuracies of various Laplacian models are compared in Fig. 11 for $s = 1/320$. As seen, those models which are reasonably accurate in regular grid structure ($N \leqslant 0$) no longer perform well in the irregular grid environment. The accuracies of these models can be improved, interestingly, by increasing the value of N to approach to that considered in the original Laplacian model ($N = 2$). Furthermore, it can be demonstrated that the accuracy of the original Laplacian model can be further refined by adopting the $N = 3$ model, in which this condition holds true within the lower range of R/s (i.e. R/s <55 in this case as shown in Fig. 11(a)). By further increasing the value of N, the accuracy,

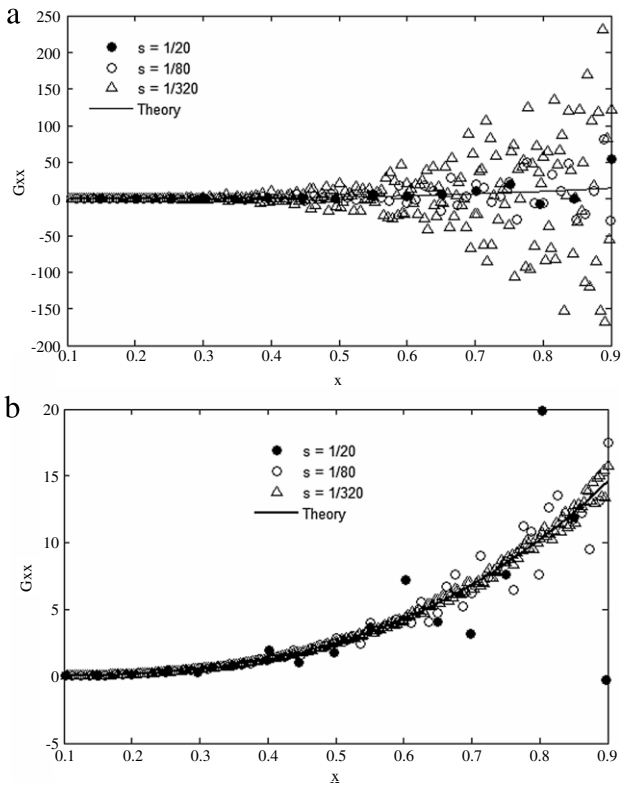

Fig. 10. Predicted Laplacian for the L1 problem by using (a) $N = 0$; (b) $N = 2$ models. Irregular grid with % of randomness =10% is used. $R = 0.1$.

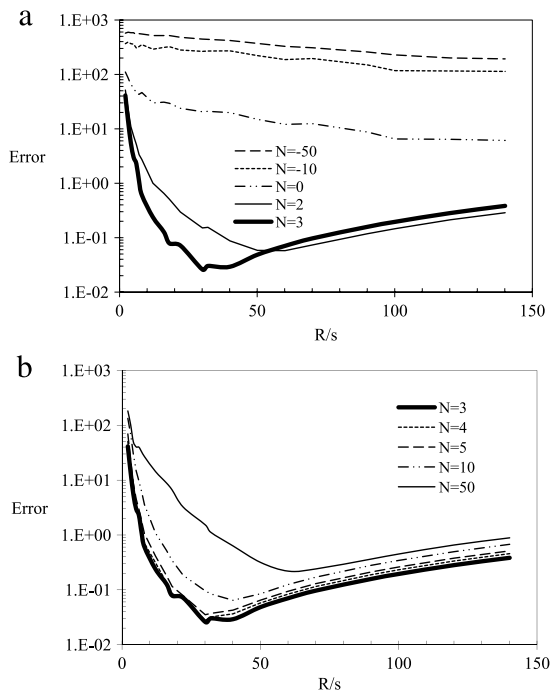

Fig. 11. Plot of errors with respect to R/s on the L1 problem for (a) $N \leqslant 3$ and (b) $N \geqslant 3$. $s = 1/320$. Irregular grid with % of randomness =10% is used.

however, turns out to be worse as shown in Fig. 11(b) for $N > 3$. Fig. 12 shows the effectiveness of $N = 3$ model in suppressing, to certain extent, the wiggles generated from the conventional $N = 0$ and $N = 2$ models.

In order to examine the effect of % of randomness (P) against the selection of N, Fig. 13 shows a series of averaged errors generated

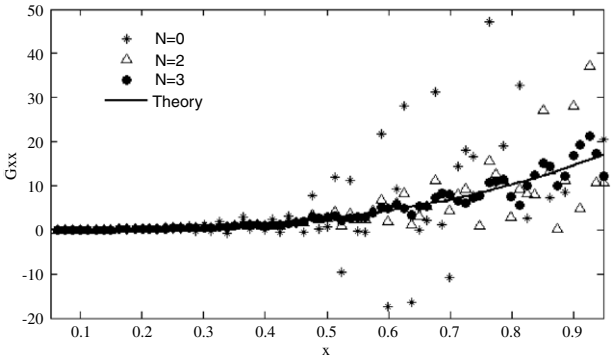

Fig. 12. Predicted Laplacian for the L1 problem on irregular grid (10% randomness). $R/s = 4.1$. $s = 1/80$.

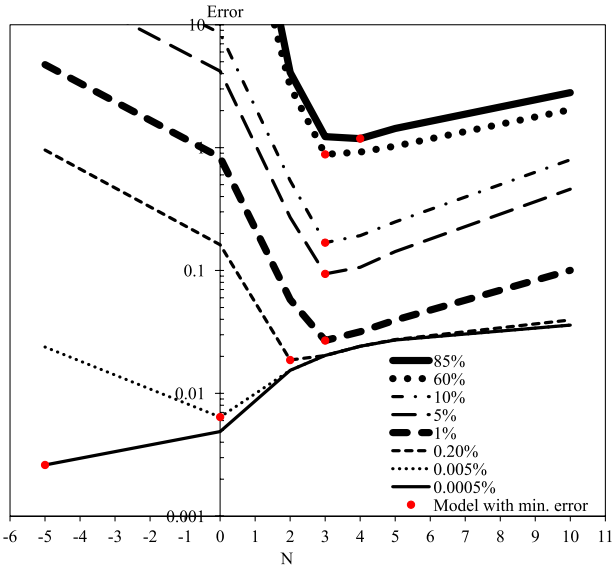

Fig. 13. Averaged error (based on 100 random grid samples) for various Laplacian models applied on the L1 problem. $s = 1/80$. $R/s = 8.1$.

from different Laplacian models applied on grids of various P. Here, the averaged errors (as defined in Section 4.1.1) are computed from 100 random grid samples and the mean value is recorded. It is important to note that the discussion above is focusing on the observations for $P = 10\%$. Seemingly, as observed from Fig. 13, $N = 3$ model is the most accurate model amongst all when $1\% < P < 60\%$ is considered. Upon increasing the % of randomness, a relatively more accurate solution can be attained from the $N = 4$ model. On the lower range of P (mildly irregular grid), as expected, the optimal value of N is shifted toward the lower end as P is approaching the regular grid structure ($P = 0$). From Fig. 13, it is straightforward to apprehend the fact that the mean error generated from a particular Laplacian model increases with respect to the % of randomness. In the current work, the predictions of Laplacian of other functions (same domain as used in L1) are performed as well and the results are tabulated in Table 1. As seen, for all the functions tested on $P = 5\%$ and $P = 10\%$, the $N = 3$ model outperforms all the other models in terms of accuracy. The distribution of error (500 random grid samples) while estimating the Laplacian of an exponential function is shown in Fig. 14. As seen, the models with $N \leqslant 0$ are suffering from wider range of errors (and higher mean error) as compared to the others. The error ranges predicted from the $N = 2$ and $N = 3$ models are almost overlapping, while the mean error of $N = 3$ model is relatively smaller than that of the $N = 2$ model.

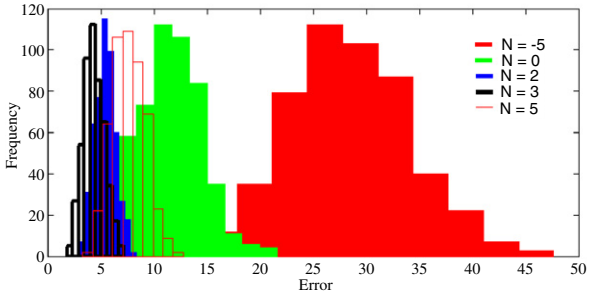

Fig. 14. Histogram of $|G_{xx} - G_{xx,abs}|/N_{int}$ for different N. Function used: $G = e^x$. $s = 1/20$. $R/s = 2.1$. $P = 10\%$. Total samples = 500.

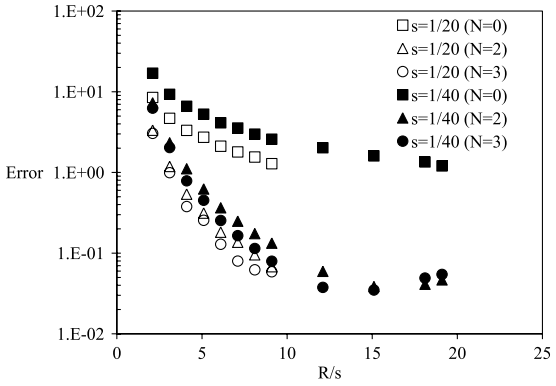

Fig. 15. Plot of averaged errors (500 random grid samples) with respect to R/s on L2 problem. Irregular grid with 10% randomness is used.

Table 1
Averaged errors (based on 500 random grid samples) predicted by various Laplacian models for different functions. $s = 1/20$; $R/s = 2.1$. $P = 5\%$ (italic value) and $P = 10\%$ are used.

N	Function				
	x	x^2	x^3	sin(x)	e^x
−5	8.98	9.02	7.94	7.65	15.15
	16.64	16.94	14.91	14.36	28.48
0	3.40	3.48	3.07	2.97	5.75
	6.84	6.92	6.12	5.81	11.72
2	1.66	1.71	1.47	1.42	2.83
	3.21	3.23	2.84	2.79	5.44
3	1.43	1.43	1.28	1.22	2.42
	2.64	2.64	2.34	2.28	4.39
5	2.47	2.49	2.22	2.13	4.16
	4.55	4.50	4.12	3.85	7.63

Next, the Laplacian on the irregular grid structure in 2D domain (L2 problem in Section 4.1.1) is evaluated at the origin ($x = 0, y = 0$). Here, the errors are averaged based on 500 random grid samples ($P = 10\%$). Again, from Fig. 15, it shows that the strategy of refining the grid spacing while retaining the R/s value is not advisable due to the generation of higher magnitude of errors. The mean error levels are generally trending downward as R/s increases, which is in contrast with that observed in those cases of regular grid. A rebound in error level can indeed be observed beyond $R/s \sim 15$ ($s = 1/40$) when $N = 2$ and $N = 3$ models are used. Fig. 16 compares the accuracies of various Laplacian models. In spite of the fact that the accuracy of the $N = 3$ model is only marginally better than the $N = 2$ model at $R/s = 2.1$, the improvement in accuracy is more noticeable as a larger R/s value is employed. Also, it is important to note from Fig. 16 that this condition holds true only when R/s is smaller than a critical value ($R/s \sim 15$), upon which the error starts to rebound.

In general, as shown in Fig. 17, $N = 4$ model seems to be attractive when $P \geqslant 50\%$. In the middle range of grid irregularity

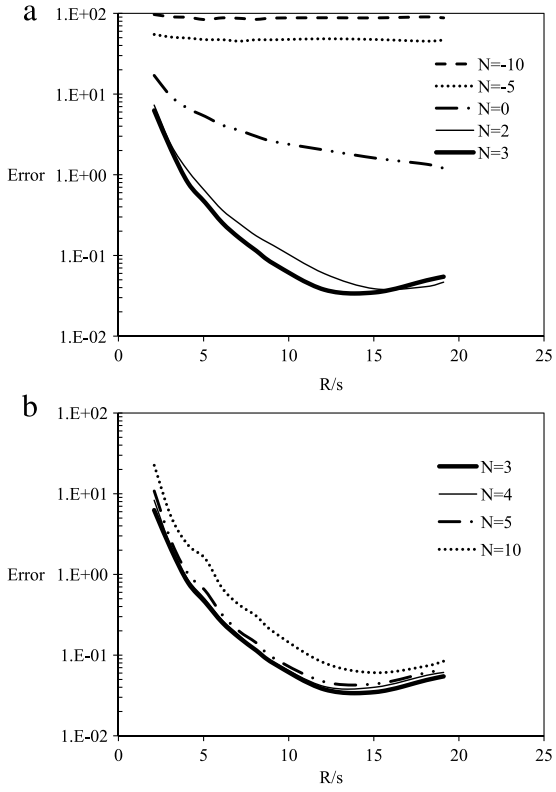

Fig. 16. Comparison of various Laplacian models on L2 problem for (a) $N \leqslant 3$ and (b) $N \geqslant 3$. Irregular grid with 10% randomness is used. $s = 1/40$.

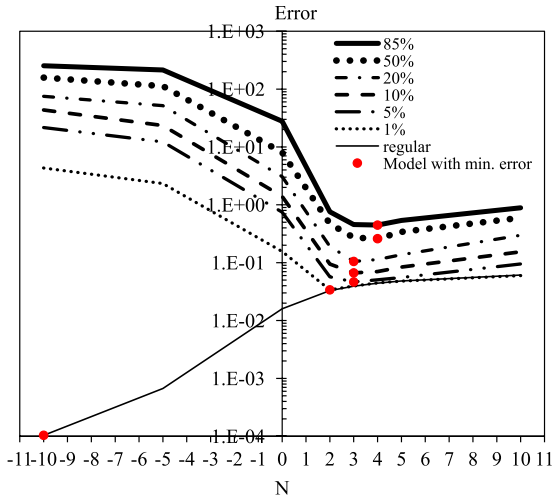

Fig. 17. Averaged error (based on 100 random grid samples) for various Laplacian models on L2 problem. $s = 1/20$. $R/s = 8.1$.

($5\% \leqslant P \leqslant 20\%$), however, the optimal N value is lowered to 3.0. As expected, this optimal N value decreases as the particles are approaching to their regular lattice positions ($P \sim 0$).

4.2. Boundary value problem

4.2.1. Regular grid

A 1D Poisson equation with varying source (BVP1 Problem) whose exact solution is $G(x) = x(x^2 - 1)/6$ is solved:

$$\frac{\partial^2 G}{\partial x^2} = x, \quad x \in [-1, 1]$$
$$G(\pm 1) = 0. \tag{16}$$

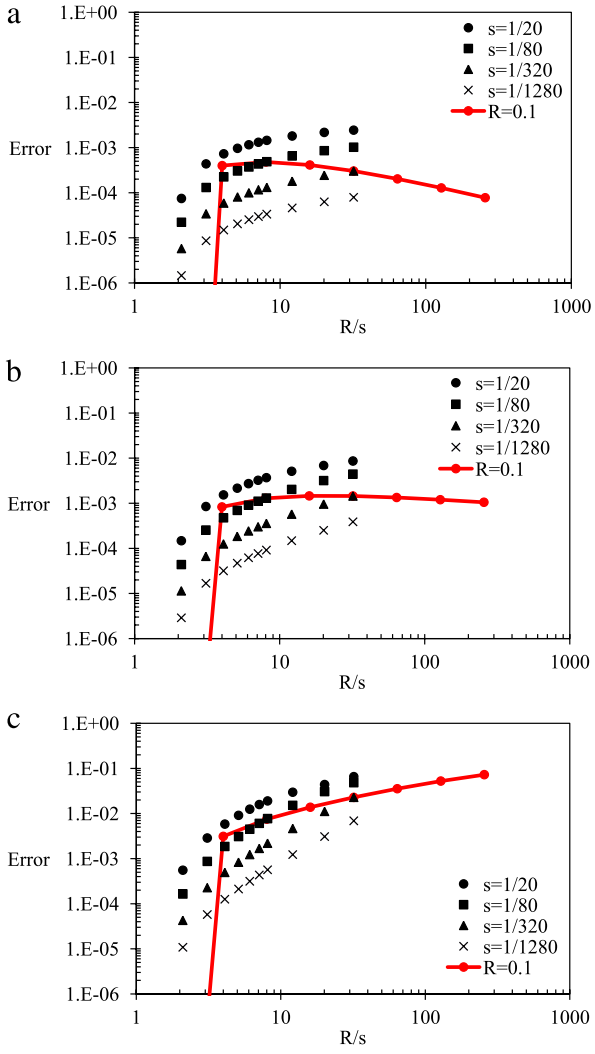

Fig. 18. Plot of errors with respect to R/s on BVP1 by using (a) $N = -1$, (b) $N = 0$ and (c) $N = 2$ models. Regular grid is used.

As seen from Fig. 18, the numerical error is reducing as the grid is refined while fixing the same number of neighbors (R/s). Generally, as expected, the error is increasing with respect to the number of neighbors employed in R for a particular grid system of spacing s. Fig. 19 compares the predicted and the theoretical solutions for various R/s. Seemingly, for $N = 2$ model, inaccuracy occurs at the boundary, and the prediction deviates considerably from the theoretical solution as R/s increases. This phenomenon is observed as well in the case of $N = -1$ model, although it is only marginal as shown in Fig. 19(b). It is worth to mention here that the derivation of the current general Laplacian model is based on the full compact support of a local particle i (see Fig. 1). Therefore, numerical errors near the Dirichlet boundary (such as free-surface) are expected if no special numerical treatment such as that proposed by Souto-Iglesias et al. [21] is implemented.

The errors while fixing $R = 0.1$ are overlaid on Fig. 18 as well at different grid spacing, proving the lack of consistency of the $N = 2$ model (Fig. 18(c)) as previously reported by Souto-Iglesias et al. [21]. As observed from Fig. 18, errors are kept to a minimum level at $R/s = 2$ (fixing $R = 0.1$), i.e. in the order of ~ -15, due to the recovery of the 2nd-order central differencing scheme. There is a sudden rise in error as R/s is increased to 4.0 while retaining the radius of influence $R = 0.1$. For $N = -1$ and $N = 0$ models, the error levels are generally descending as more neighbors (R/s) are employed (see Fig. 18(a) and (b)). The augmentation of error

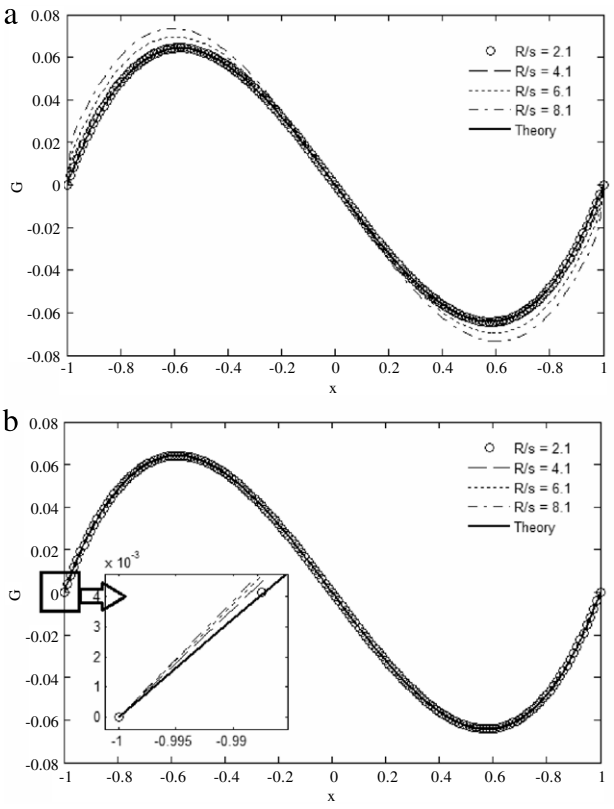

Fig. 19. Predicted solution G by using (a) $N = 2$ and (b) $N = -1$ models on BVP1 at various R/s. Regular grid with $s = 1/80$ is used.

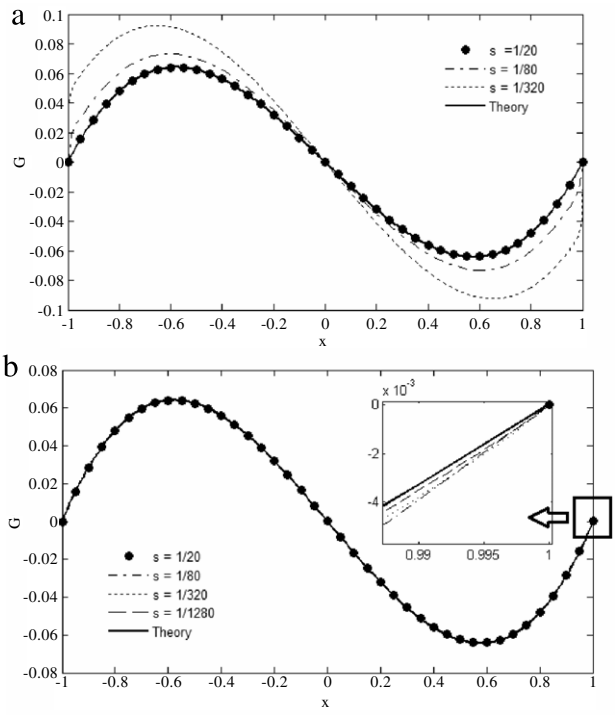

Fig. 20. Predicted solution G on a regular grid by using (a) $N = 2$ and (b) $N = -1$ models on BVP1. $R = 0.1$.

as observed in $N = 2$ model (Fig. 18(c)) is in fact due to the discontinuity occurred at the boundary as the grid is refined (see Fig. 20(a)) for the case of $N = 2$, while it is not truly significant for the case of $N = -1$ (Fig. 20(b)). The general comparison of

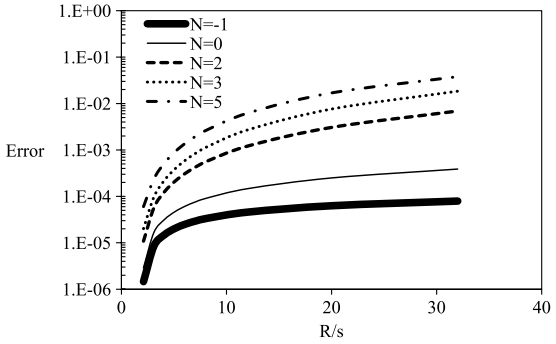

Fig. 21. Comparison of various Laplacian models for BVP1 at the regular grid spacing $s = 1/1280$.

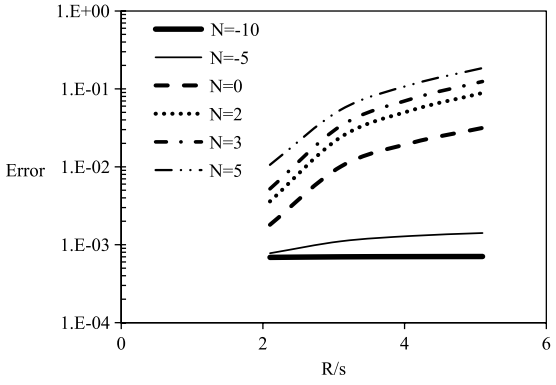

Fig. 22. Comparison of various Laplacian models for BVP2 at the regular grid spacing $s = 1/20$.

accuracies for various Laplacian models is reported in Fig. 21 for the case of fine grid spacing $s = 1/1280$. Again, it demonstrates the effectiveness of those models with smaller N for the entire range of R/s, mainly due to the smaller leading error concluded from the modified equation analysis.

Next, the Laplacian models are applied on a 2D Poisson equation where the exact solution is $G(x, y) = \sin(\pi x)\cos\left(\frac{\pi}{2}y\right)$(BVP2):

$$\begin{aligned} &\frac{\partial^2 G}{\partial x^2} + \frac{\partial^2 G}{\partial y^2} = -\frac{5}{4}\pi^2 \sin(\pi x)\cos\left(\frac{\pi}{2}y\right); \quad x \in [-1, 1]; \\ &\quad y \in [-1, 1] \\ &G(\pm 1, y) = G(x, \pm 1) = 0. \end{aligned} \tag{17}$$

As deduced from Fig. 22, again, for the entire range of R/s, a better accuracy can be attained when the Laplacian model of smaller N is considered. The solutions at various locations in the 2D domain are plotted in Fig. 23, showing that the solutions obtained from the Laplacian model with smaller N exhibit better agreement with the theoretical ones.

4.2.2. Irregular grid

Fig. 24 shows the numerical errors generated from various Laplacian models upon solving the BVP1 on irregular grid spacing with $P = 10\%$. In general, at low R/s, the original Laplacian model ($N = 2$) performs considerably well as compared to the other models. Due to the inconsistency at the boundaries, those models with higher value of N ($N \geqslant 2$) exhibit increasing level of error as the number of neighbors (R/s) increases. Upon surpassing a critical R/s value, it is interesting to note that those models with $N = 0$ and $N = -1$, in which their accuracies are expected to be inferior in irregular grid environment, are now exhibiting increasing accuracy

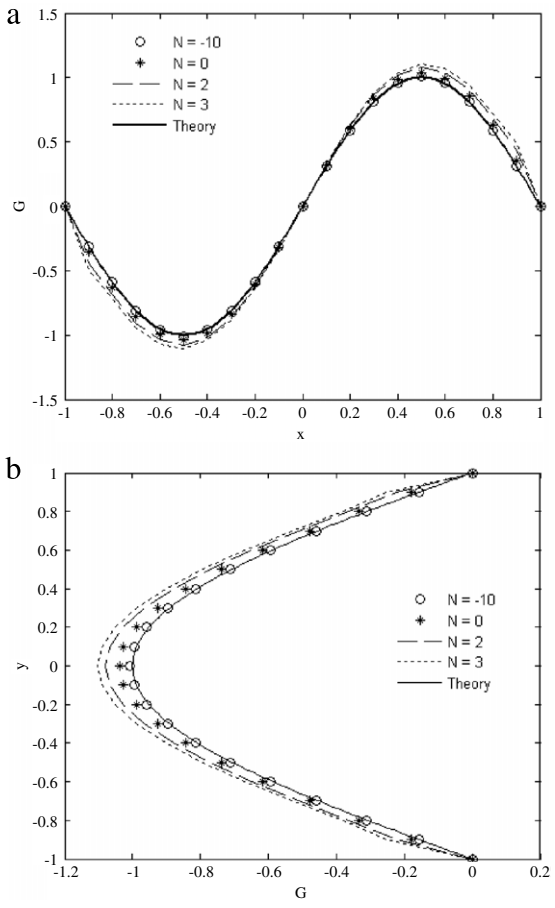

Fig. 23. Predicted solution of BVP2 on a regular grid at (a) $y = 0$ and (b) $x = -0.5$. $s = 0.1$. $R/s = 3.1$.

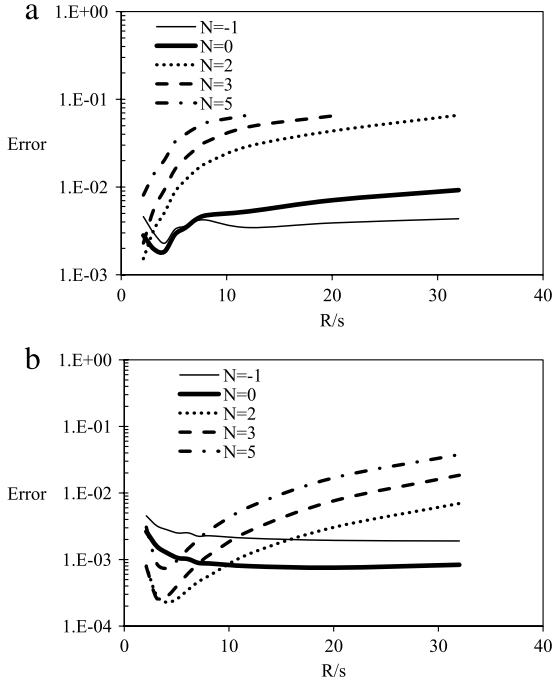

Fig. 24. Comparison of various Laplacian models for BVP1 using (a) $s = 1/20$ and (b) $s = 1/1280$. Irregular grid of 10% randomness is used.

than the original Laplacian model. This critical R/s value, in general, increases as a finer particle system is employed as shown in

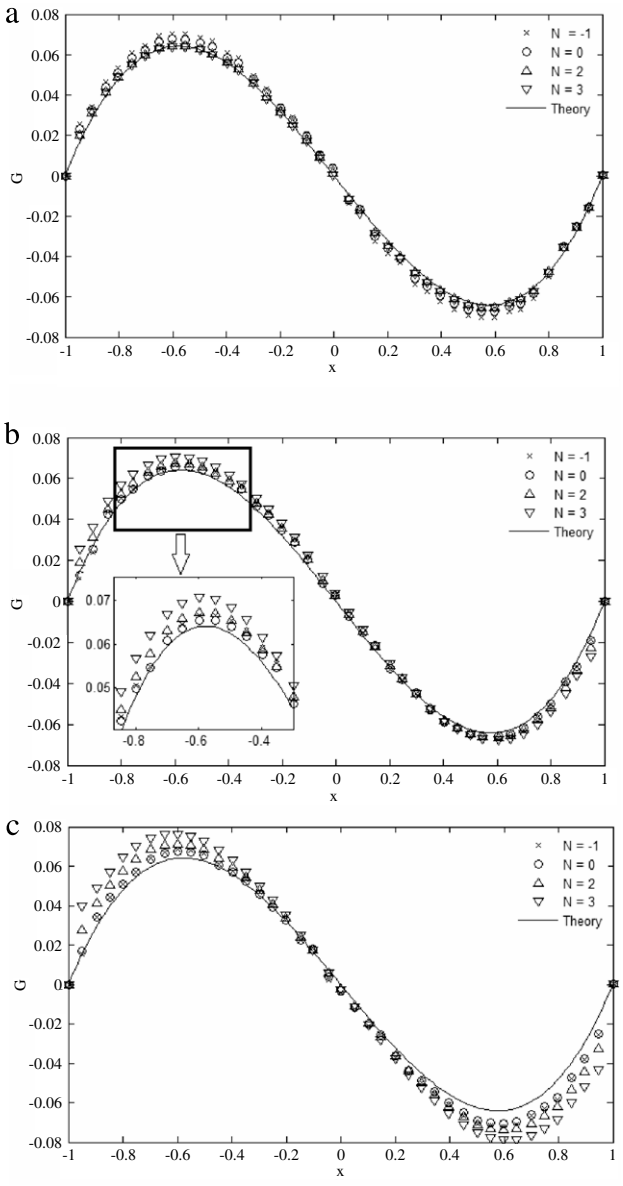

Fig. 25. Predicted solution G for BVP1 by using (a) $R/s = 2.1$; (b) $R/s = 3.1$ and (c) $R/s = 4.1$. $s = 1/20$. Irregular grid with 10% randomness is used.

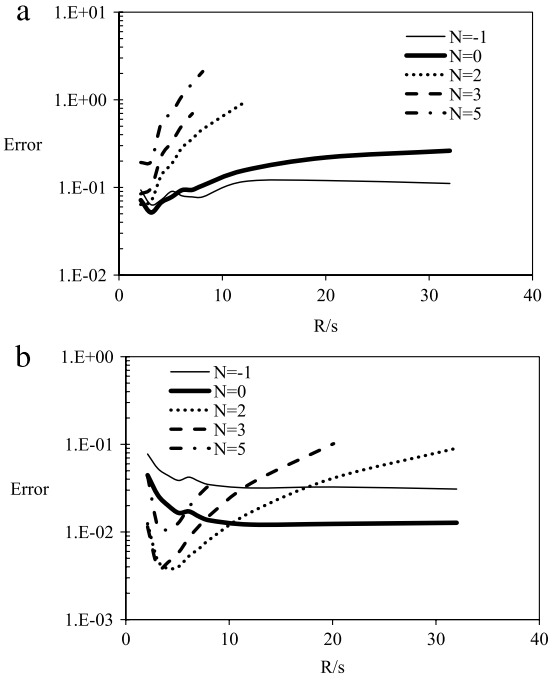

Fig. 26. Comparison of Laplacian models on BVP3 for (a) $s = 1/20$ and (b) $s = 1/1280$. Irregular grid of 10% randomness is used.

Fig. 24(b). In order to examine this phenomenon, Fig. 25 shows the solutions obtained from various Laplacian models at different R/s. At $R/s = 2.1$, the predictions from $N = 2$ and $N = 3$ models are quite close to the theoretical ones as compared to those of $N \leqslant 0$ shown in Fig. 25(a). Upon increasing R/s to 3.1 (Fig. 25(b)), one is able to observe an abrupt change in the solution profile near the boundaries for $N = 2$ and $N = 3$ models, while those models with $N \leqslant 0$ still somehow preserve the smoothness of solution near the boundaries. Due to the elliptic nature of the Poisson equation, this will inevitably degrade the accuracies of the solutions generated from those $N \geqslant 2$ models in the interior region. By further increasing R/s to 4.1 (Fig. 25(c)), as expected, the accuracies of $N \geqslant 2$ models near the boundaries are severely affected, and those solutions of $N \leqslant 0$ models are now in better agreement with the theoretical data. Nevertheless, their accuracies are still not comparable with that of the original Laplacian model when a small R/s value, i.e. $R/s = 2.1$, is employed.

Next, the Poisson equation subjected to mixed Dirichlet and Neumann boundary conditions (BVP3) whose exact solution is $G(x) = x^2$ is considered:

$$\begin{aligned} &\frac{\partial^2 G}{\partial x^2} = 2, \quad x \in [0, 1] \\ &G'(0) = 0 \\ &G(1) = 1. \end{aligned} \tag{18}$$

This problem is very similar to the Poisson equation of pressure in MPS, whereby the Dirichlet condition prevails at the free surface and the Neumann condition (zero pressure gradient) is applied at the wall boundary. Here, the Neumann boundary condition for BVP3 problem is implemented by introducing the ghost particles on the left boundary having the same value (determined implicitly) as that of $G(x = 0)$, and the number of ghost particles is dependent on the value of R employed. Fig. 26 compares the accuracies of various models on an irregular grid system of 10% randomness. Again, the superiority in accuracy of the $N = 2$ model at low R/s as compared to those $N = 0$ and $N = -1$ models is no longer sustainable as the number of neighbors increases. Similar behavior can be observed in the 2D problem (BVP2) as reported in Fig. 27.

The solutions for the BVP3 problem are plotted in Fig. 28 at various R/s. Again, the solution obtained from the $N = 2$ model shows the closest agreement with the theoretical solution when $R/s = 2.1$ is employed. As R/s is increased to 4.1, some discrepancies start to occur at the right boundary where Dirichlet boundary condition prevails, which is further magnified when $N > 2$. Owing to this reason, the $N = 0$ and $N = -1$ models, which are less susceptible to profile disruption near the Dirichlet boundary, tend to be more accurate than the original Laplacian model ($N = 2$) when higher R/s is considered.

Fig. 29 shows that the optimal Laplacian model in solving a BVP may deviate if the % of randomness varies. Generally, as the % of randomness increases, the optimal value of N will be augmented as well. Here, the errors are averaged over 100 random grid samples for 2D problem (BVP2) and 500 random samples for 1D problems (BVP1 and BVP3). As expected, as the irregularity decreases ($P \to 0$), the accuracies of those $N < 0$ models will become more prominent.

Table 2
Grid convergence analysis on $G''(x) = x^2 + 2$ for (a) regular grid and (b) irregular grid ($P = 20\%$). For (b), errors are averaged over 100 samples. $x \in [0, 1]$. $G'(0) = 0$, $G(1) = 1$. For meshless scheme, $R/s = 2.0$.

P	Grid size	$N = 0$		$N = 2$		FVP		FDM1		FDM2		FVM (Cell centered)	
		Error	Rate	Error	Rate	Error	Rate	Error	Rate	Error	Rate	Error	Rate
(a)													
0%	0.1	4.95E−02	–	4.95E−02	–	4.95E−02	–	4.95E−02		5.42E−04	–	3.19E−03	–
	0.05	2.49E−02	0.99222	2.49E−02	0.99222	2.49E−02	0.99222	2.49E−02	0.99222	1.37E−04	1.98162	7.98E−04	1.99924
	0.025	1.25E−02	0.99605	1.25E−02	0.99605	1.25E−02	0.99605	1.25E−02	0.99605	3.45E−05	1.99090	2.00E−04	1.99981
	0.0125	6.24E−03	0.99801	6.24E−03	0.99801	6.24E−03	0.99801	6.24E−03	0.99801	8.65E−06	1.99547	4.99E−05	1.99995
	0.00625	3.12E−03	0.99900	3.12E−03	0.99900	3.12E−03	0.99900	3.12E−03	0.99900	2.17E−06	1.99774	1.25E−05	1.99999
	0.003125	1.56E−03	0.99946	1.56E−03	0.99933	1.56E−03	0.99950	1.56E−03	0.99950	5.42E−07	1.99887	3.12E−06	2.00000
p	Grid size	$N = 0$		$N = 2$		$N = 3$		$N = 4$		FVP		FVM (Cell centered)	
		Error	Rate	Error	Rate	Error	Rate	Error	Rate	Error	Rate	Error	Rate
(b)													
20%	0.1	2.38E−01	–	1.02E−01	–	1.10E−01	–	1.54E−01	–	9.02E−02	–	3.27E−03	–
	0.05	2.25E−01	0.07753	7.59E−02	0.42443	6.06E−02	0.86288	9.02E−02	0.77228	6.76E−02	0.41713	8.25E−04	1.98897
	0.025	2.23E−01	0.01123	5.82E−02	0.38378	4.59E−02	0.40204	6.59E−02	0.45209	6.22E−02	0.11957	2.06E−04	2.00291
	0.0125	2.16E−01	0.04795	5.08E−02	0.19456	3.76E−02	0.28483	5.48E−02	0.26678	5.86E−02	0.08639	5.15E−05	1.99872
	0.00625	2.12E−01	0.02733	4.74E−02	0.10077	3.10E−02	0.27838	4.89E−02	0.16441	5.62E−02	0.06107	1.29E−05	2.00045
	0.003125	2.10E−01	0.01373	4.53E−02	0.06524	2.70E−02	0.20011	4.36E−02	0.16398	5.47E−02	0.03882	3.22E−06	1.99978

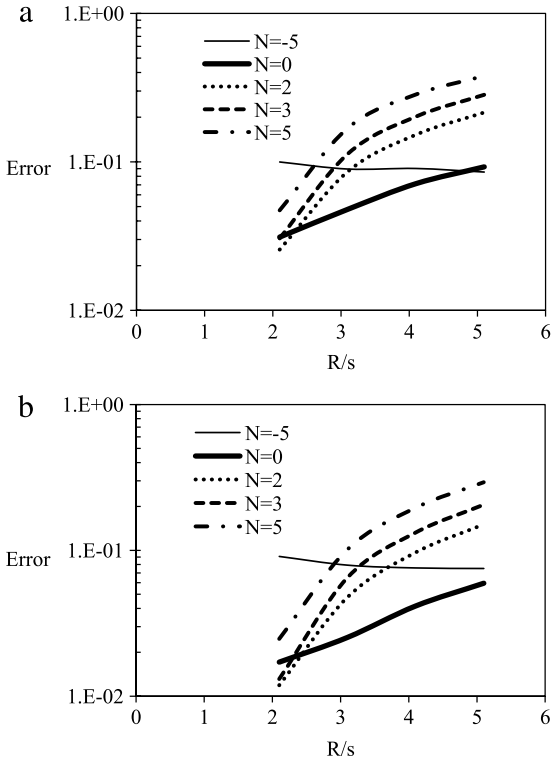

Fig. 27. Comparison of Laplacian models on BVP2 for (a) $s = 1/5$ and (b) $s = 1/10$. Irregular grid of 10% randomness is used.

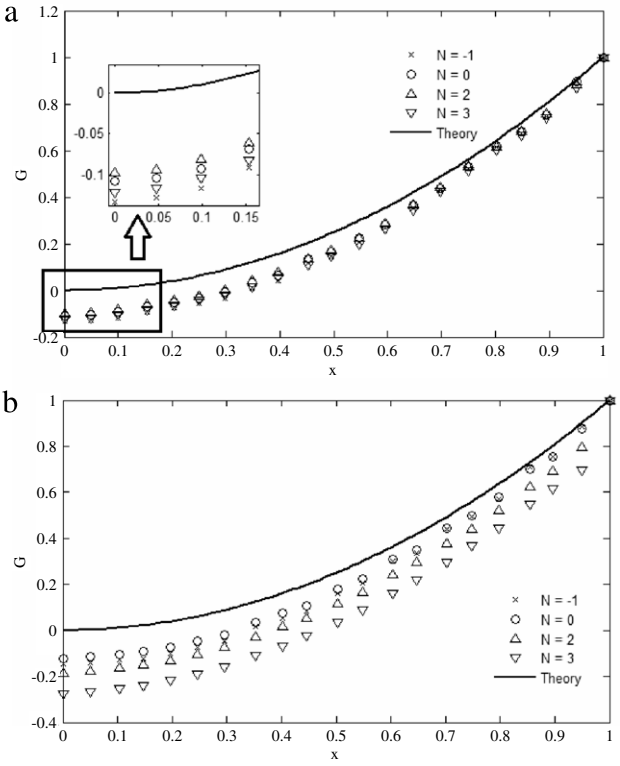

Fig. 28. Predicted solution G for BVP3 by using (a) $R/s = 2.1$ and (b) $R/s = 4.1$. $s = 1/20$. Irregular grid with 10% randomness is used.

4.2.3. Spatial convergence

From the solution of boundary value problems, it is interesting to note that the error is decreasing as the grid is refined even in cases employing random grid structure. This important numerical property, however, is not observed while evaluating the Laplacian of a field variable as noticed in Section 4.1.2. Due to the elliptic behavior of the BVP, we speculate that the solutions are strongly confined by the boundary conditions, which is helpful in suppressing the discretization errors of Laplacian terms.

The rates of spatial convergence for the 2D problem subjected to Dirichlet boundary condition (BVP2) are plotted in Fig. 30. Here, the rates of spatial convergence are computed based on the grid spacing $s = 1/5k$, where $k = 1, 2, 4, 8$. For cases employing irregular grids, the L1-error norms are averaged over 10 random grid samples. As expected, for a particular Laplacian model, the rate of spatial convergence decreases as the % of randomness increases. Seemingly, as the irregular grids are employed, the rate of spatial convergence has a local maximum value at $N*$ (marked in red shown in Fig. 30) within the range considered: $-1 < N < 5$. In general, $N*$ is shifted to the upper end as a highly irregular grid is employed. Similar observations are found for BVP1 and BVP3 (results not shown here).

Table 2(a) compares the rates of spatial convergence of various numerical schemes for BVP3 problem (mixed Neumann and Dirichlet boundary conditions with a non-linear source term:

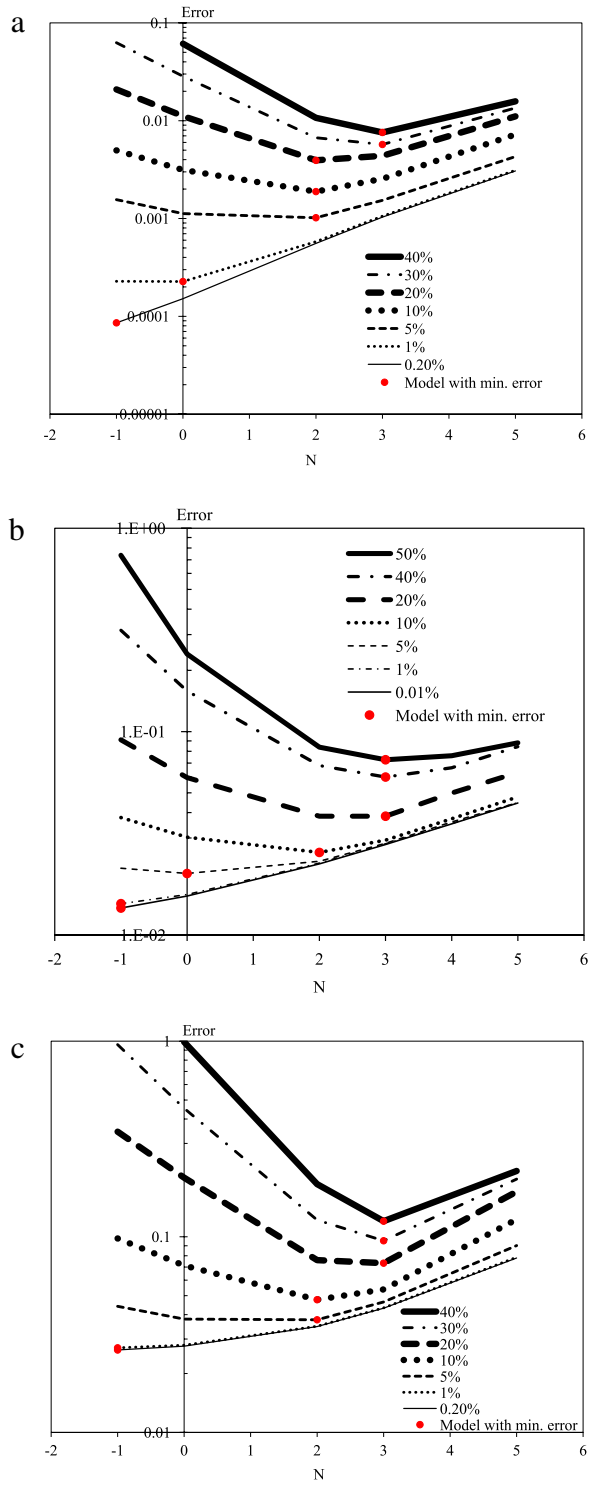

Fig. 29. Averaged errors for various Laplacian models employing grid of different % of randomness. (a) BVP1; $s = 1/20$; 500 irregular grid samples, (b) BVP2; $s = 1/5$; 100 irregular grid samples and (c) BVP3; $s = 1/20$; 500 irregular grid samples. $R/s = 2.1$.

$x^2 + 2$ in this case) on regular grid. A first-order approximation is used to approximate the Neumann condition at $x = 0$ for Finite Difference Method (FDM1). The rate of spatial convergence of FDM1 can be enhanced by using a 2nd-order approximation at the Neumann boundary (FDM2) or the cell-centered Finite Volume Method (FVM). Due to the nature of the implementation of Neumann boundary condition at $x = 0$ in the current meshless procedure, it can be easily understood that the accuracies of the

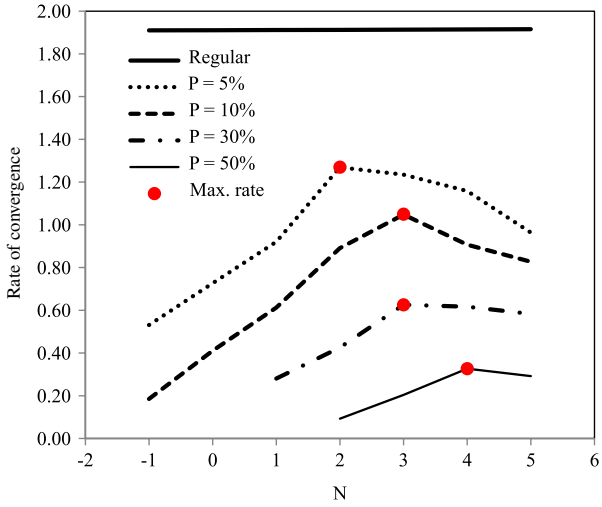

Fig. 30. Rates of spatial convergence of BVP2 at different % of randomness P. For irregular grids, the L1-norm errors are averaged over 10 irregular grid samples. $R/s = 2.0$.

meshless procedures considered in the current work such as MPS and Finite Volume Particle (FVP) [36] are only $O(s)$.

As reported from Table 2(b), a reduction of rate of spatial convergence of a meshless scheme can be observed when grid irregularity is introduced. This shortcoming is quite noticeable when the $N = 0$ model is considered. The FVP scheme can be used to improve the rate of spatial convergence of $N = 0$ model; despite of this, the effectiveness of FVP scheme may not on par with those of the original MPS Laplacian ($N = 2$) and $N = 3$ models. Seemingly, the second-order spatial convergence of FVM is not significantly affected in the irregular grid environment. Table 3 reports the grid convergence analysis for the BVP considered in Table 2, whereby the Dirichlet boundary condition prevails at $x = 0$ ($G(0) = -1/12$) in this case. For $R/s = 2.0$, the meshless methods (e.g. MPS and FVP) are equivalent to the second-order Central Differencing Scheme, in which their accuracies are now $O(s^2)$ on regular grid. Again, the accuracy of $N = 0$ model can be improved by the Laplacian models such as $N = 2$ and $N = 3$ when irregular grid is employed.

4.3. Flow problem

Finally, the lid-driven flow in a square cavity of width W ($u_{lid} = 1.0$ m/s; $W = 1.0$ m; $\rho = 1.0$ kg/m^3; $Re = 100$) is solved by employing a recently developed particle method whereby the pressure term is treated as a field variable and stored in an Eulerian mesh [37]. The Laplacian operator as proposed in the current work is used to evaluate the flow diffusion term at the scattered particles, in which their motions are computed in a Lagrangian manner. The pressure gradient on each fluid particle (not a material point, merely acting as an observation point) is evaluated by using a simple shape function and no artificial treatments are employed to avoid particle clustering as commonly employed in a particle-based solver. Fig. 31 shows the instantaneous pressure field and particles' speed at different time instants. The simulation is carried out until $t = 50$ s to ensure that a nearly stationary solution is achieved. Fig. 32 shows the time evolution of velocities at different points. Seemingly, the solutions obtained from $N = 2$ and $N = 3$ models are less wiggling than those of $N = 0$ model.

Fig. 33(a) compares the horizontal velocity (u-velocity) profiles predicted at the vertical mid-section of the cavity on 40×40 background mesh. The $N = 0$ model seems to have over-predicted the horizontal velocities near the bottom wall, while the numerical

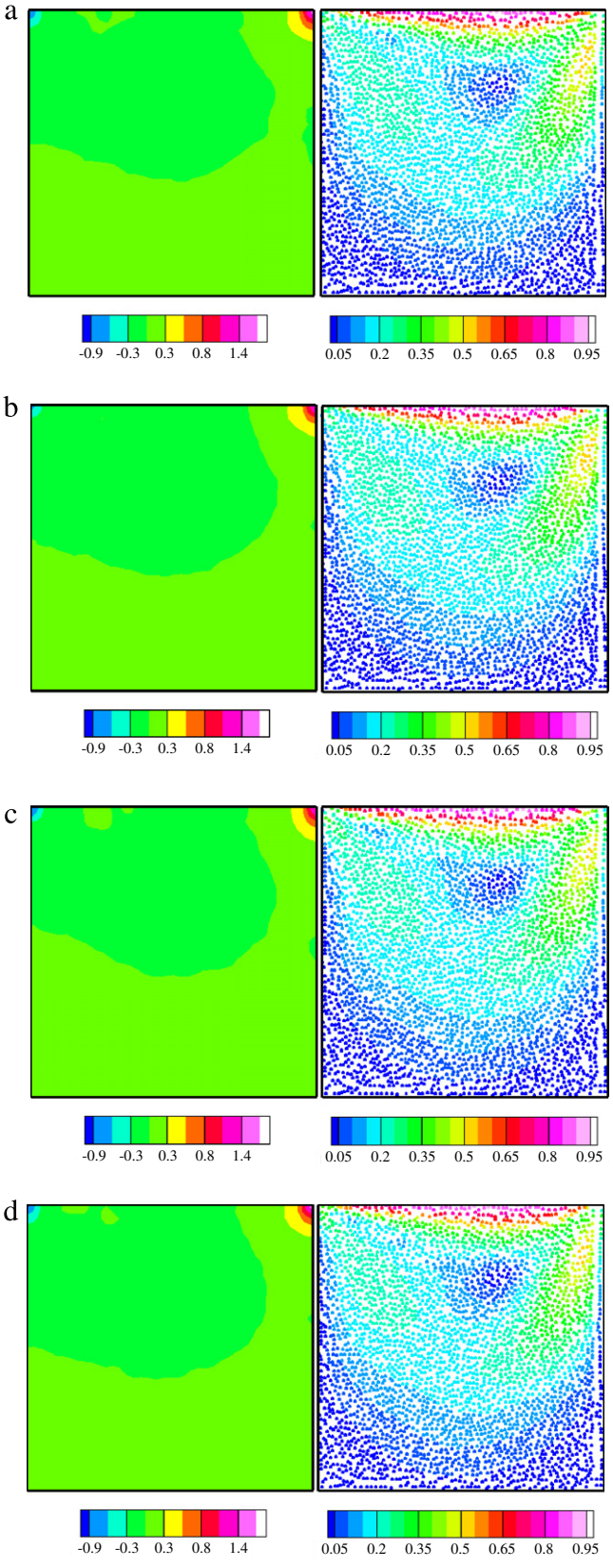

Fig. 31. Instantaneous pressure field on a background pressure mesh 40 × 40 [Pa] (left) and particles' speed [m/s^2] (right) in the lid-driven flow problem at (a) $t = 47$ s; (b) $t = 48$ s; (c) $t = 49$ s and (d) $t = 50$ s. $N = 2$.

solutions from the other two models ($N = 2$ and $N = 3$) are quite close to the fine grid steady-state solution of Erturk and Dursun [38] in the vicinity of the bottom wall. However, all models tend to under-predict the horizontal velocities at the core region, and it seems from Fig. 33(b) that the use of finer mesh resolution (80 × 80) does not provide a significant improvement in this regard.

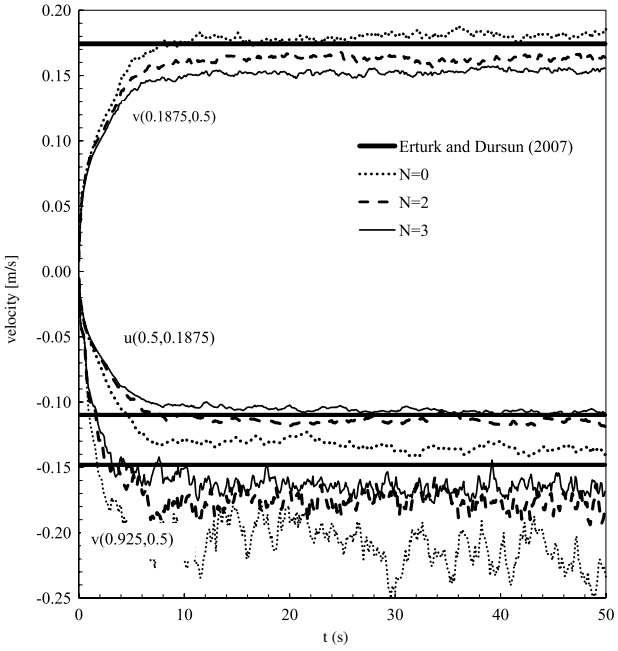

Fig. 32. Time evolution of velocities at various locations for a lid-driven flow problem. Mesh 40 × 40.

Concerning on the spatial variation of vertical velocity (v-velocity) along the horizontal mid-section of the cavity as shown in Fig. 33(c) on 40 × 40 mesh, the $N = 0$ model is able to provide a better representation on the overshoot seen in the left compartment of the cavity. However, the spatial extent of the positive vertical velocity has been slightly over-predicted by the $N = 0$ model. Furthermore, the undershoot value predicted by the $N = 0$ model at $x \sim 0.85$ m has remarkably surpassed the reference solution as well. Amongst the Laplacian models studied, the solution of the $N = 2$ model seems to agree quite well with the reference solution. And, it is worth to mention here that the resulting solution becomes more smeared as N is increased to 3. Upon increasing the mesh resolution to 80 × 80 as reported in Fig. 33(d), there is a noticeable improvement of the $N = 0$ solution, particularly in resolving the overshoot and undershoot of the velocity profile. The solutions of $N = 2$ and $N = 3$ models are quite similar, except that the value of the undershoot predicted by the $N = 3$ model comes closer to that of the $N = 0$ model.

5. Conclusion

Stemming from the mathematical work by Isshiki [7] in detailing the theoretical background of MPS-based differential operators, a general MPS-based Laplacian model has been put forward in the current work. It has been found that the original Laplacian model and the Zhang's model can indeed be deduced from the general model reported in the current work. Modified equation analysis has further revealed that there exists a class of Laplacian models ($N < 0$) which are more accurate than the conventional MPS Laplacian models in regular grid environment. Following are the major findings from the current work:

1. For the explicit computation of Laplacian term on regular interior grids, better accuracy can be achieved by further

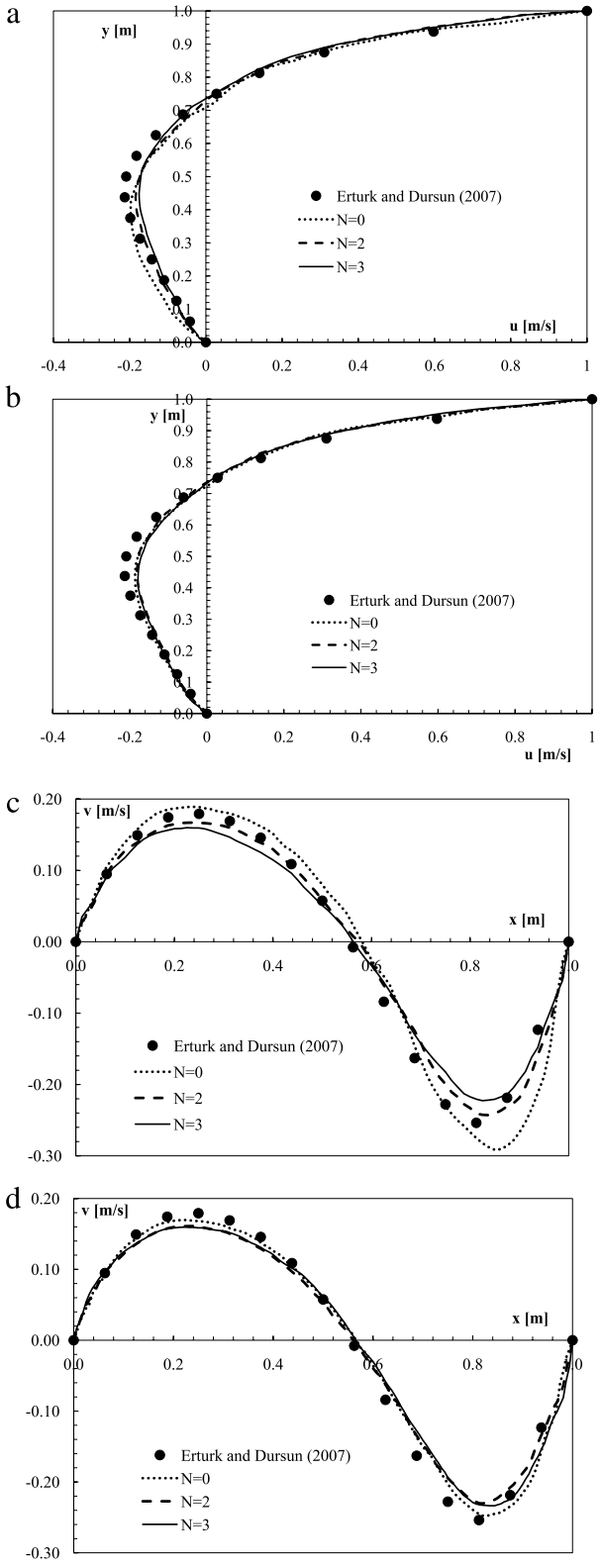

Fig. 33. Comparison of velocity profiles at the mid-sections of the cavity. (a) u-velocity on 40×40 mesh; (b) u-velocity on 80×80mesh; (c) v-velocity on 40×40 mesh; (d) v-velocity on 80×80mesh.

refining the grid spacing s while retaining the number of neighbors in a particular radius of influence R. Deterioration in accuracy will occur, however, as R is further increased while fixing the grid spacing. In general, better accuracy can be achieved when a Laplacian model with smaller N is employed. This has led to the reasoning on why the Zhang's model ($N = 0$) is more preferable than the original Laplacian model ($N = 2$) in the case of regular grids.

2. For the explicit computation of Laplacian term on irregular interior grids, the strategy of refining the grid spacing while retaining the number of neighbors in a particular radius of influence R is no longer applicable due to the numerical errors generated from the artificial velocity terms. If the case of fine grid spacing is desirable, the corresponding parameter controlling the number of neighbors (i.e. R/s) must be increased for attaining a reasonable accurate solution. As the % of randomness increases, the optimal N value in promoting solution accuracy increases. In an irregular grid environment, the original Laplacian model ($N = 2$) is generally more accurate than the Zhang's model ($N = 0$) in evaluating the Laplacian term, which may justify on its wider application in MPS for simulating flow particles undergoing random motions.
3. Concerning on solving the Boundary Value Problem (BVP) in regular grid structure, again, a more accurate solution can be attained via the Laplacian model with smaller N. However, cases employing large number of neighbors are not recommended, as solution accuracy can be degraded as R increases due to the mathematical inconsistency at the Dirichlet boundary (resulting in solution discontinuity). This may be attributed to the nature of the current general Laplacian model, whereby it is derived based on the full compact support of a local particle i (see Fig. 1).
4. The mathematical inconsistency at the Dirichlet boundary can be found as well in the case of solving the BVP in irregular grid structure. At low R/s (=2.1), however, the solutions provided by the original Laplacian model ($N = 2$) are still acceptable for grid irregularity of 10% and appear to be more accurate than those of $N \leqslant 0$ and $N \geqslant 3$ models. Again, this study has revealed that as the % of randomness increases, the optimal N value in ensuring higher global accuracy and spatial rate of convergence will increase correspondingly.
5. The optimal value of N is dependent on the degree of grid irregularity, which is prescribed beforehand in the pure diffusion problems considered in the current work. In a practical flow problem, the degree of grid irregularity may vary from one location to another, signifying that the optimal value of N may differ within the flow domain. This has been witnessed from our flow results presented in the current work, whereby it is difficult to deduce a model (with a sole parameter N) which is globally accurate throughout the flow domain. In the context of irregular grid, it seems that the original Laplacian model is sufficient for simulating fluid flow. From our point of view, the artificial velocity terms AV_x and AV_y appeared in Eq. (14), which are written as a function of particle topology, serve as a more meaningful way to describe grid irregularity. We speculate that these terms can be eliminated to enhance the accuracy of a Laplacian model. This will be reported in our future work.

Acknowledgments

The authors wish to thank the anonymous reviewers for their constructive comments. Also, the financial supports provided by the Ministry of Education Malaysia (Fundamental Research Grant Scheme Ref. No: FRGS/2/2013/TK01/UNITEN/02/1) and the Ministry of Science, Technology and Innovation (MOSTI) Malaysia (Project No: 06-02-03-SF0258) are greatly acknowledged.

Table 3
Grid convergence analysis on $G''(x) = x^2 + 2$ for (a) regular grid and (b) irregular grid ($P = 20\%$). For (b), errors are averaged over 100 samples. $x \in [0, 1]$. $G(0) = -1/12$, $G(1) = 1$. For meshless scheme, $R/s = 2.0$.

P	Grid size	$N = 0$		$N = 2$		FVP		FDM		FVM (Cell centered)	
		Error	Rate	Error	Rate	Error	Rate	Error	Rate	Error	Rate
(a)											
0%	0.1	1.25E−04	–	1.25E−04	–	1.25E−04	–	1.25E−04	–	2.98E−03	–
	0.05	3.30E−05	1.92200	3.30E−05	1.92200	3.30E−05	1.92200	3.30E−05	1.92200	7.46E−04	1.99918
	0.025	8.46E−06	1.96253	8.46E−06	1.96253	8.46E−06	1.96253	8.46E−06	1.96253	1.87E−04	1.99980
	0.0125	2.14E−06	1.98162	2.14E−06	1.98162	2.14E−06	1.98162	2.14E−06	1.98162	4.67E−05	1.99995
	0.00625	5.39E−07	1.99090	5.39E−07	1.99090	5.39E−07	1.99090	5.39E−07	1.99090	1.17E−05	1.99999
	0.003125	1.35E−07	1.99547	1.35E−07	1.99547	1.35E−07	1.99546	1.35E−07	1.99547	2.92E−06	2.00000

P	Grid size	$N = 0$		$N = 2$		$N = 3$		$N = 4$		FVP		FVM (Cell centered)	
		Error	Rate	Error	Rate	Error	Rate	Error	Rate	Error	Rate	Error	Rate
(b)													
20%	0.1	5.27E−02	–	2.17E−02	–	2.29E−02	–	3.16E−02	–	2.82E−02	–	3.05E−03	–
	0.05	5.36E−02	–	1.48E−02	0.54918	1.29E−02	0.82478	2.38E−02	0.41000	1.95E−02	0.52802	7.66E−04	1.99335
	0.025	5.32E−02	0.00974	1.29E−02	0.19932	1.00E−02	0.36532	1.91E−02	0.31531	1.54E−02	0.34466	1.92E−04	1.99861
	0.0125	5.31E−02	0.00336	1.15E−02	0.16282	8.23E−03	0.28539	1.45E−02	0.39943	1.44E−02	0.09850	4.79E−05	2.00093
	0.00625	5.26E−02	0.01195	1.13E−02	0.02846	7.70E−03	0.09673	1.25E−02	0.20976	1.42E−02	0.01336	1.20E−05	1.99807
	0.003125	5.40E−02	–	1.12E−02	0.00704	6.94E−03	0.14837	1.15E−02	0.12823	1.39E−02	0.03092	3.00E−06	2.00081

References

[1] S. Koshizuka, A. Nobe, Y. Oka, Numerical analysis of breaking waves using the moving particle semi-implicit method, Internat. J. Numer. Methods Fluids (1998) 751–769.
[2] A. Khayyer, H. Gotoh, Development of CMPS method for accurate water-surface tracking in breaking waves, Coast. Eng. J. 50 (2) (2008) 179–207.
[3] A. Khayyer, H. Gotoh, Enhancement of stability and accuracy of the moving particle semi-implicit method, J. Comput. Phys. 230 (2011) 3093–3118.
[4] N. Tsuruta, A. Khayyer, H. Gotoh, A short note on dynamic stabilization of moving particle semi-implicit method, Comput. & Fluids 82 (2013) 158–164.
[5] S. Koshizuka, H. Tamako, Y. Oka, A particle method for incompressible viscous flow with fluid fragmentation, J. Comput. Fluid Dyn. 4 (1995) 29–46.
[6] G.T. Duan, B. Chen, Stability and accuracy analysis for viscous flow simulation by the moving particle semi-implicit method, Fluid Dyn. Res. 45 (035501) (2013) 1–15.
[7] H. Isshiki, Discrete differential operators on irregular nodes (DDIN), Internat. J. Numer. Methods Engrg. 88 (2011) 1323–1343.
[8] C.H. Hu, M. Sueyoshi, Numerical simulation and experiment on dam break problem, J. Mar. Sci. Appl. 9 (2010) 109–114.
[9] Y.X. Zhang, DC. Wan, Application of MPS in 3D dam breaking flows, Sci. Sin. Phys, Mech & Astro 41 (2) (2011) 140–154.
[10] S. Koshizuka, Y. Oka, Advanced analysis of complex thermal-hydraulic phenomena using particle method. GENES4/ANP2003, Sep 15–19, 2003, Kyoto, Japan, Paper 1165.
[11] M. Asai, H. Nijo, K. Ito, Simulation of the impingement of a liquid jet on a molten iron bath by using a particle method, ISIJ International 49 (2) (2009) 178–181.
[12] M. Sueyoshi, Numerical simulation of extreme motions of a floating body by MPS Method. OCEANS '04, MTTS/IEEE TECHNO-OCEAN '04 2004; 1: 566–572.
[13] H. Maeda, K. Nishimoto, K. Masuda, T. Asanuma, M.M. Tsukamoto, T. Ikoma, Numerical analysis for hydrodynamic motions of floating structure using MPS method. Proceedings of OMAE 2004: 23rd International Conference on Offshore Mechanics and Arctic Engineering, Vancouver, Canada, 20–25 June 2004, Paper OMAE2004-51435.
[14] M. Sueyoshi, M. Kashiwagi, S. Naito, Numerical simulation of wave-induced nonlinear motions of a two-dimensional floating body by the moving particle semi-implicit method, J. Mar. Sci. Tech. 13 (2008) 85–94.
[15] K.C. Ng, E.Y.K. Ng, Laminar mixing performances of baffling, shaft eccentricity and unsteady mixing in a cylindrical vessel, Chem. Eng. Sci. 15 (2013) 960–974.
[16] K.C. Ng, E.Y.K. Ng, WH. Lam, Lagrangian simulation of steady and unsteady laminar mixing by plate impeller in a cylindrical vessel, Ind. Eng. Chem. Res. 52 (2013) 10004–10014.
[17] D. Barada, M. Itoh, T. Yatagai, Computer simulation of photoinduced mass transport on azobenzene polymer films by particle method, J. Appl. Phys. 96 (8) (2004) 4204–4210. 2004.
[18] S. Zhang, K. Morita, N. Shirakawa, K. Fukuda, Simulation of the Rayleigh–Taylor instability with the MPS method, Mem. Fac. Eng. Kyushu Univ. 64 (4) (2004) 215–228.
[19] H. Ichikawa, S. Labrosse, Smooth particle approach for surface tension calculation in moving particle semi-implicit method, Fluid Dyn. Res. 42 (035503) (2010) 1–18.
[20] A. Shakibaeinia, Y.C. Jin, A mesh-free particle model for simulation of mobile-bed dam break, Adv. Water Resour. 34 (2011) 794–807.
[21] A. Souto-Iglesias, F. Macia, L.M. Gonzalez, JL. Cercos-Pita, On the consistency of MPS, Comput. Phys. Comm. 184 (2013) 732–745.
[22] S. Zhang, K. Morita, K. Fukuda, N. Shirakawa, Simulation of the incompressible flows with the MPS method. 13th International Conference on Nuclear Engineering, Beijing, China, May 16–20, 2005. Paper No: ICONE 13-50166.
[23] S. Zhang, K. Morita, K. Fukuda, N. Shirakawa, An improved MPS method for numerical simulations of convective heat transfer problems, Internat. J. Numer. Methods Fluids 51 (2006) 31–47.
[24] S. Zhang, K. Morita, K. Fukuda, N. Shirakawa, Simulation of three-dimensional convection patterns in a Rayleigh–Benard system using the MPS Method, Mem. Fac. Eng. Kyushu Univ. 66 (1) (2006) 29–37.
[25] Z.G. Sun, Y.Y. Liang, G. Xi, Numerical simulation of the flow in straight blade agitator with the MPS method, Internat. J. Numer. Methods Fluids 67 (2011) 1960–1972.
[26] Z.G. Sun, G. Xi, Numerical study of pressure wave transmission in liquid under different interface conditions using particle method. Proceedings of the ASME 2009 Fluids Engineering Division Summer Meeting, FEDSM2009, August 2–6, 2009, Vail, Colorado USA. Paper No: FEDSM2009-78201.
[27] G. Yoshikawa, K. Hirata, F. Miyasaka, Y. Okaue, Numerical analysis of transitional behavior of ferrofluid employing MPS method and FEM, IEEE Trans. Magn. 47 (5) (2011) 1370–1373.
[28] G. Yoshikawa, K. Hirata, F. Miyasaka, Numerical analysis of electromagnetic levitation of molten metal employing MPS method and FEM, IEEE Trans. Magn. 47 (5) (2011) 1394–1397.
[29] Y. Chikazawa, Development of a particle method for elastic and creep deformation. 18th International Conference on Structural Mechanics in Reactor Technology (SMiRT 18), Beijing, China, August 7–12, 2005. Paper no: SMiRT 18-B01-3.
[30] N. Hirata, K. Anzai, Numerical simulation of shrinkage formation of pure Sn casting using particle method, Mater. Trans. 52 (10) (2011) 1931–1938.
[31] T.W.H. Sheu, C.P. Chiao, C.L. Huang, Development of a particle interaction kernel function in MPS method for simulating incompressible free surface flow, J. Appl. Math. 31 (2011) Article ID 793653: 16 pages.
[32] C.L. Huang, T.W.H. Sheu, Development of a moving and stationary mixed particle method for solving the incompressible Navier–Stokes equations at high Reynolds numbers, Numer. Heat Transfer, Part B 62 (2012) 71–85.
[33] C.L. Huang, T.W.H. Sheu, Development of an upwinding particle interaction kernel for simulating incompressible Navier–Stokes equations, Numer. Meth. Partial Differ. Equ. 28 (2012) 1574–1597.
[34] A. Khayyer, H. Gotoh, A higher order Laplacian model for enhancement and stabilization of pressure calculation by the MPS method, Appl. Ocean Res. 32 (2010) 124–131.
[35] A. Khayyer, H. Gotoh, A 3D higher order Laplacian model for enhancement and stabilization of pressure calculation in 3D MPS-based simulations, Appl. Ocean Res. 37 (2012) 120–126.
[36] L.C. Guo, S. Zhang, K. Morita, K. Fukuda, Fundamental validation of the finite volume particle method for 3D sloshing dynamics, Internat. J. Numer. Methods Fluids 6 (2012) 1–17.
[37] YH. Hwang, A moving particle method with embedded pressure mesh (MPPM) for incompressible flow calculations, Numer. Heat Transfer, Part B 60 (2011) 370–398.
[38] E. Erturk, B. Dursun, Numerical solutions of 2-D steady incompressible flow in a driven skewed cavity, ZAMM Z. Angew. Math. Mech. 87 (2007) 377–392.